A computational methodology to account for the liquid film thickness evolution in Direct Numerical Simulation of prefilming airblast atomization

R. Payri, F.J. Salvador, M. Carreres [*], C. Moreno-Montagud

CMT-Motores Térmicos, Universitat Politècnica de València, Camino de Vera s/n, E-46022, Spain

ARTICLE INFO

ABSTRACT

Prefilming airblast atomization is becoming widely used in current aero engines. Fundamental studies on the actual annular configuration of airblast atomizers are difficult to realize. For this reason, researchers have also focused on planar configurations. In this regard, the Karlsruhe Institute of Technology (KIT) developed a test rig to conduct experimental activities, conforming a large database with results for different working fluids and operating conditions. Such data allow two-phase flow modelers to validate their calculations concerning primary atomization on these devices. The present investigation proposes a Direct Numerical Simulation (DNS) study on the KIT planar configuration through the Volume of Fluid (VOF) method within the PARIS Simulator code. The novelty compared to DNS works reported in the literature resides in the use of a boundary condition that allows accounting not only for the gas inflow turbulence but also for the spatio-temporal evolution of the liquid film thickness at the DNS inlet and its related effect on turbulence. The proposed methodology requires computing precursor single-phase and two-phase flow Large-Eddy Simulations on the prefilmer flow, with the assumption that the flow between computational domains is one-way coupled. Results are compared to DNS that only account for a constant (both timewise and spanwise) liquid film thickness at the domain inlet, validating the full methodology workflow. The proposed methodology is shown to improve the qualitative description of the atomization mechanism, as the different stages of breakup (liquid accumulation behind the prefilmer edge, bag formation, bag breakup, ligament formation and ligament breakup) coexist spanwise for a given temporal snapshot. This implies a more continuous atomization than the one predicted by the constant film thickness case, which showed the same breakup stage to be present along the prefilmer span for a given instant and led to a more discretized set of atomization events. The proposed workflow allows quantifying the influence of the liquid film flow evolution above the prefilmer surface on primary breakup frequency and relevant atomization features.

1. Introduction

The aviation industry produces a not negligible part of the global pollutant emissions, due to its important growth in the last decades (Valdés et al., 2019). This problem gets worse because combustion residues at high altitudes of the troposphere are more harmful to the environment than they are at sea level (Søvde et al., 2014). In order to lower the emissions, new engine concepts and combustion technologies are required. In this context, lean combustion emerges to improve fuel consumption and emissions, but requiring high control of the process to avoid flameout (Liu et al., 2017). For this reason, the research community has increased their interest in the atomization process, as controlling combustion in aero engines highly depends on this phenomenon.

Some of the most commonly used atomizers in the aviation industry are pressure-swirl atomizers and prefilming airblast atomizers (Lefebvre and McDonell, 2017). In the former, liquid fuel is brought into the environment and atomized by means of a pressure difference. In the latter, in turn, the fuel is first deposited onto a prefilmer and then driven by a surrounding high-velocity airstream towards an atomizing edge. When the liquid reaches this edge, a shear instability appears on the film, it breaks up into ligaments and subsequently disintegrates into droplets. This study focuses on this last type of atomizers.

Some groups have performed experimental studies on actual annular configurations of airblast atomizers. Jasuja (2006) compared low- and high-shear design philosophies over a wide range of ambient air densities and kerosene flow rates at an ambient air temperature using Phase Doppler Interferometry and laser sheet imaging. Matsuura et al. (2008) investigated the effects of p_a on SMD for a counter double-swirl

Nomenclature

Abbreviatures

CFD	Computational Fluid Dynamics
CFL	Courant–Friedrichs–Lewy number
CLSMOF	Coupled Level-Set Moment of Fluid
CLSVOF	Coupled Level-Set Volume of Fluid
CSF	Continuum Surface Force
DMD	Dynamic Mode Decomposition
DNS	Direct Numerical Simulation
eDNS	embedded Direct Numerical Simulation
ELSA	Eulerian–Lagrangian Spray Atomization
FCT	Flux-Corrected Transport
FVM	Finite Volume Method
GAMG	Geometric Agglomerated Algebraic Multi-Grid
HF	Height Function
ICM	Interface Capturing Methods
KIT	Karslruhe Institute of Technology
LDA	Laser Doppler Anemometry
LES	Large-Eddy Simulation
MULES	Multidimensional Universal Limiter for Explicit Solution
PAMELA	Primary Atomization Model for prEfilming airbLAst injectors
PARIS	PArallel, Robust, Interface Simulator
PDA	Phase Doppler Anemometry
PDF	Probability Density Function
PISO	Pressure-Implicit with Splitting of Operators
PLIC	Piecewise Linear Interface Calculation
POD	Proper Orthogonal Decomposition
RMS	Root Mean Square
SGS	Sub-grid Scale
SMD	Sauter Mean Diameter
SPH	Smoothed Particle Hydrodynamics
TE	Trailing Edge
VOF	Volume of Fluid
VTK	The Visualization Toolkit
WALE	Wall Adapting Local Eddy-viscosity

Greek symbols

α	Liquid volume fraction
δ	Boundary layer thickness
δ_S	Dirac delta function
κ	Interface curvature
λ	Liquid film wavelength
μ	Dynamic viscosity
ν	Kinematic viscosity
ρ	Density
σ	Surface tension
θ	Liquid-wall contact angle

List of notations

$\dot{V}$	Volumetric flow rate
$\mathbf{f}_\sigma$	Surface tension force vector
$\mathbf{n}$	Interface normal vector
$\mathbf{u}_c$	Compression velocity vector

$\mathbf{u}_{def}$	Film deformation velocity
$\mathbf{u}_{lig}$	Mean ligament tip velocity vector
$\mathbf{u}_{str}$	Ligament tip velocity vector
$\mathbf{u} = (u, v, w)$	Velocity vector
$\mathbf{x} = (x, y, z)$	Position vector
b	Prefilmer span
C_α	Interface artificial compression coefficient
d_V	Droplet volumetric diameter
f_{bu}	Mean breakup frequency
f_{film}	Liquid film wave frequency
f_{main}	Frequency among main bag breakup events
g_c	Cell grading coefficient
h_c	Prefilmer channel height
h_l	Liquid film thickness
h_p	Prefilmer edge thickness
L_f	Effective prefilming length
L_p	Prefilmer length
L_x	DNS domain length
L_y	DNS domain height
L_z	DNS domain width
l_η	Kolmogorov length scale
L_{bu}	Mean breakup length
L_{str}	Ligament length
M	Momentum flux ratio
Oh	Ohnesorge number
p	Pressure
r	Density ratio
Re	Reynolds number
Re_τ	Frictional Reynolds number
T	Temperature
t	Time
u_m	Average streamwise velocity at the DNS inlet
V	Volume
We	Weber number
y^+	Non-dimensional boundary layer distance

high-shear-type fuel injector at different air pressure drops, kerosene flow rates and AFR than Jasuja (2006), using Phase Doppler Anemometry and laser sheet Mie scattering visualization. Gepperth et al. (2014) explored the coupling of the film flow and primary breakup process for an industrial prefilming airblast nozzle through high speed shadowgraphy. Two advanced mathematical procedures were used for the first time to analyze the high resolution recordings of such atomizers: proper orthogonal decomposition (POD) and dynamic mode decomposition (DMD). Results revealed an independence between the extracted frequency of the precessing vortex core, film waves and atomization events for this range of operating conditions. In addition, a linear behavior of the film flow dynamics was observed from the DMD analysis.

Nevertheless, the annular configuration of the airblast atomizer poses a multi-scale nature problem and presents some geometrical complexity, importantly hindering its study. In this sense, many researchers have focused their efforts on planar configurations, which are much simpler but allow extrapolating conclusions to the actual annular configurations due to an analogy by similarity, as pointed out by Berthoumieu and Lavergne (2001) and confirmed by Holz et al. (2016).

Focusing on the planar configuration, several test rigs have been developed to study the primary breakup in airblast atomizers, generally using an airfoil-shaped solid section as a prefilmer. Inamura
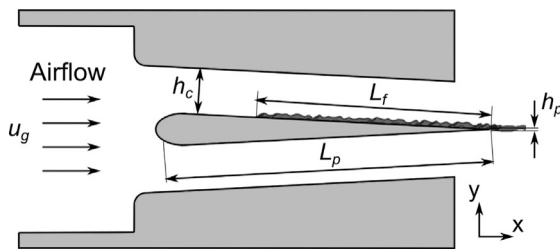
Fig. 1. Sketch of the KIT-ITS test rig cross-section.

et al. (Inamura et al., 2012, 2019) used this sort of test rig with water as a working fluid under different operating conditions, establishing the primary breakup mechanism of these devices. Matas et al. (2015) used a similar setup to study the shear instability of a planar air–water mixing layer, demonstrating the direct influence of gas turbulence on this instability and showing that mean gas flow quantities do not fully characterize its features. The test rig in KIT-ITS (Gepperth et al., 2010), in turn, stands out as it has been used to carry out tests with diverse operating conditions and fuels through a variety of techniques, providing a huge experimental database. In this particular model, the airflow is divided into two ducts by the mentioned airfoil-shaped solid section (as shown in Fig. 1) and the fuel is injected through some holes equally distributed spanwise close to the leading edge of the upper surface. The fuel then develops as a planar liquid film reaching the atomizing edge.

A first set of experimental studies reported in the KIT-ITS test rig were conducted by Gepperth et al. (2010, 2012). For a varied range of operating conditions (fluids, flow rates, prefilmer geometrical dimensions, ...), the influence of many parameters in primary atomization has been studied at ambient pressure and temperature using shadowgraphy, PDA measurements and ligament tracking. The results showed a strong dependence of the mean droplet diameter on mean air velocity and atomizing edge thickness, these being the dominant parameters. Prefilming length, liquid physical properties and liquid volume flow rate had a weaker effect, but still affected the ligament formation process. From these results, correlations were derived to predict the breakup frequency, Sauter Mean Diameter (SMD) and mean droplet velocities in the primary atomization region. Unlike previously existing models, their correlation did not require knowledge of film properties, which are difficult to estimate.

In addition to those steady air flow experiments, Chaussonnet et al. (2017, 2018) carried out similar tests at ambient temperature and pressure but with fluctuating air flow instead, again using shadowgraphy and LDA velocimetry. A pulsating device generated velocity fluctuations of certain amplitude and frequency, corresponding to usual observed magnitudes in real combustion chambers. Results reported a significant influence on SMD up to a certain frequency, that is, a non-linear transfer function with a low-pass filter type of behavior.

Results were later extended to higher ambient pressures through new experiments by Chaussonnet et al. (2020). The aerodynamic stress $\rho_g u_g^2$ was used instead of the ambient pressure as a more appropriate parameter to characterize prefilming airblast breakup, and the domain was virtually split into several atomizing cells with single ligaments. Besides, two new characteristic lengths were proposed: one based on atomizing cell streamwise surface, related to the air velocity; and another one related to film loading, which showed a correlation with the SMD. This is in line with the idea from all previous works that liquid accumulation is key to determine the primary spray characteristics. Many correlations from the literature were compared with these experiments, most of them underestimating SMD in their predictions. This emphasizes the need of calibrating models using experimental techniques like shadowgraphy (Payri et al., 2020).

As experimental studies are expensive and involve specialized facilities and resources, many researchers have delved into Computational

Fluid Dynamics (CFD) to model primary atomization in pursuit of accuracy at lower costs. Chaussonnet et al. (2016) studied the prefilming airblast atomizer geometry through Large Eddy Simulations (LES) to compare with (Gepperth et al., 2014, 2012) experimental results. They developed the Primary Atomization Model for prEfilming airbLAst injectors (PAMELA) and implemented it into the LES solver AVBP. Considering the experimental observations, the droplet size distribution followed a Rosin–Rammler function with both scale and shape parameters depending on flow properties. The PAMELA model links these parameters with two Weber numbers based on the thickness of the atomizing edge and the boundary layer on the prefilmer (We_{h_p} and We_δ) and an extra function of h_p, obtaining five constants that are independent from the flow conditions. After calibration of these constants, they were able to predict mean and RMS velocity profiles, capture the vortex shedding downstream of the atomizing edge and the drop size Probability Density Function (PDF) of the spray with moderate computational effort. Palanti et al. (2021) also carried out LES of the study case, coupling Interface Capturing Methods (ICM) with the Eulerian–Lagrangian Spray Atomization (ELSA) approach with the OpenFOAM open source code. Their objective was to catch the main features of the breakup mechanisms with a low-intensity computational strategy and a novel postprocessing technique, relating curvature of the liquid interface to the PDF function.

To get a better understanding of the atomization process, other authors opted for Direct Numerical Simulations (DNS) as they can provide detailed information hardly achievable by current optical techniques. Nevertheless, accurate DNS of a full prefilming airblast atomizer geometry are unreasonable with current computational resources, even assuming the planar configuration simplification. To overcome this limitation, these authors relegated the domain to the last part of the prefilmer and the primary breakup zone.

Mukundan et al. (2019a) and Braun et al. (2019) used constant velocity profiles for both the liquid and gas phases at the inlet boundary conditions, gaining some insight on the breakup mechanisms. However, Sauer et al. (Sauer et al., 2014, 2016) and Warncke et al. (2017) introduced the concept of embedded DNS (eDNS). In this methodology some precursor LES are carried out in order to generate realistic boundary conditions for the gas phase at the DNS inlet. This way, the turbulent fluctuations of velocities are stored in planes that serve as input data for the final target simulation. Warncke et al. (2019) specifically showed a strong influence of such turbulent inflow condition on the primary breakup process. Jiang and Ling (Jiang and Ling, 2020, 2021) later presented a work particularly devoted to analyzing the impact of gas turbulence intensity on the development and breakup of interfacial waves, demonstrating an effect of inlet gas turbulence on wave breakup location, dominant mode of breakup and size distribution of the resultant droplets. The method used in the latter works to solve the gas–liquid interface is the Volume Of Fluid (VOF), in which an indicator function represents the liquid volume contained in a cell (Torregrosa et al., 2020; Payri et al., 2022). The advantage of this method is its inherent mass conservation, at the cost of interface smearing. Carmona et al. (2021) used the incompressible solver NGA combining the VOF method with the Piecewise Linear Interface Calculation (PLIC) technique for interface reconstruction to study the KIT-ITS configuration, properly replicating the breakup mechanism while maintaining a limited CPU consumption.

Level-Set methods have also been used by other authors, but hybridizing them with the VOF method in the so-called CLSVOF (Zandian et al., 2017; Agbaglah et al., 2017; Mukundan et al., 2019a, 2022) or with the Moment of Fluid method (CLSMOF) (Mukundan et al., 2019b, 2022) in order to counter the mass conservation limitations of the former and capture interface topology.

On the other hand, Lagrangian methods have also been used to model primary breakup in prefilming airblast atomizers. In particular, Smoothed Particle Hydrodynamics (SPH) has been successfully used in 2D (Koch et al., 2017; Holz et al., 2018) and 3D (Braun et al.,
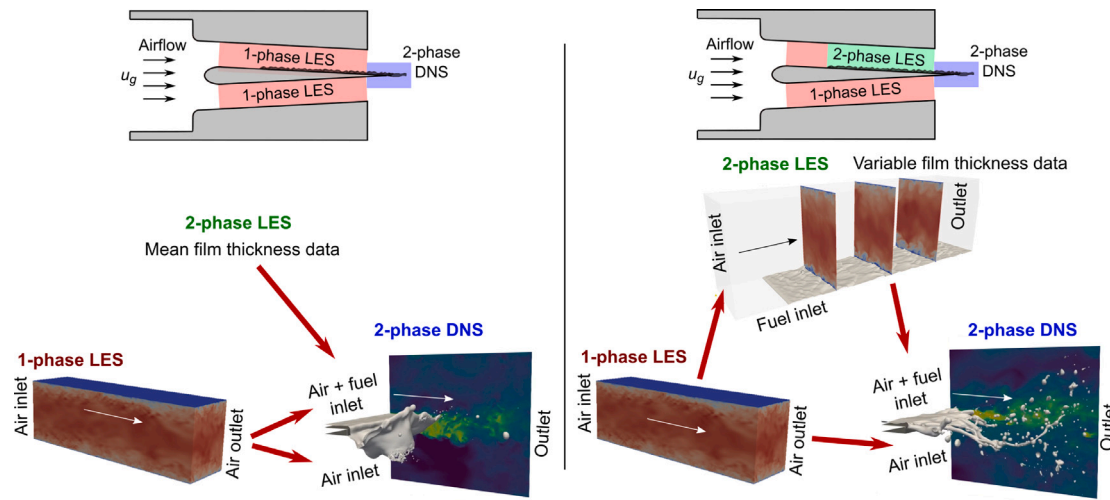
Fig. 2. Simulation workflow to account for gas inflow turbulence and a constant liquid film thickness at the DNS inlet (left) and proposed workflow to account for the liquid film thickness evolution at the DNS inlet (right).

2019) planar configurations. Being a meshfree method, it allows a significantly lower computational cost than grid-based simulations. This advantage is reduced when a high number of particles need to be tracked. As a drawback, the interpolation accuracy is influenced by particle arrangement.

The main objective of the present work is to develop a numerical workflow to account for the spatio-temporal variations of the liquid film thickness on a planar prefilmer at the inlet of the atomizer edge DNS, analyzing their effect on primary atomization predictions. To this end, the eDNS concept from Sauer et al. (2014) is first adopted as a baseline configuration to account for gas inflow turbulence. Section 2 sketches this numerical workflow explaining how this concept is extended by adding the computation of two-phase precursor LES of the flow on the prefilmer. The particular case of study is also explained in this section. Then, Section 3 describes the details for the numerical resolution of each simulation. Additionally, this section details the post-processing methods used to extract information from the ligaments and droplets shaped during breakup. This includes a method to characterize the ligaments not only in the streamwise direction (usual procedure to validate against literature shadowgraphy data), but in the 3D domain. This approach constitutes another main contribution of the investigation to the state of the art. Results are shown in Section 4, including the validation of the precursor simulations and a discussion on the DNS data from a qualitative and a quantitative standpoint. Finally, the main findings of the manuscript are described in Section 5.

2. Proposed simulation workflow and case study

The particular planar airblast atomizer to be studied was presented in Fig. 1, corresponding to the KIT-ITS test rig (Gepperth et al., 2010). As stated in Section 1, this investigation relies on the eDNS concept by Sauer et al. (2014) to account for gas inflow turbulence at the atomizing edge DNS as a starting point, with a constant liquid film thickness at the DNS inlet. Fig. 2 (left) depicts the simulation workflow used to replicate this approach, where it can be seen that a precursor single-phase LES is needed reproducing the channel flow above and below the prefilmer surface. Time-varying velocity data from this simulation are mapped to the inlet of the subsequent DNS, restricted to the last part of the prefilmer and a short distance downstream of its edge. This DNS will hereinafter be referred to as *Constant h_l DNS* or $h_l \neq f(t,z)$ *DNS*. Please note that care is taken so that the LES data passed on to both sides of the prefilmer surface of the DNS are not synchronized. Fig. 2 (right), in turn, shows the proposed simulation workflow to extend the method to account for temporal and spatial liquid film waves on the

Table 1
Cases of study corresponding to the strategies used to supply data to the inlet boundary condition of the atomizing edge DNS.

Case	Description	Air velocity	Liquid velocity	Film thickness
$h_l \neq f(t,z)$	Constant h_l DNS	Variable	Constant	Constant
$h_l = f(t,z)$	Time-varying h_l DNS	Variable	Variable	Variable

Table 2
Geometrical parameters of the planar prefilmer from the KIT-ITS test rig (Gepperth et al., 2010).

Description	Parameter	Value [mm]
Length	L_p	70.9
Span	b	50
Edge thickness	h_p	0.23
Channel height	h_c	8.11
Effective film length	L_f	47.6

prefilmer that could influence breakup. In this case, the single-phase LES velocity data only feed the lower part of the DNS inlet, being also mapped to an additional two-phase flow precursor LES that simulates the film evolution above the prefilmer. Hence, the liquid boundary layer is developed as it would do through the prefilmer surface. Time-varying velocity and liquid volume fraction results of this simulation are then mapped to the upper part of the DNS inlet obtaining not only a variable airstream velocity but also a variable velocity and height of the liquid film. Consequently, such DNS will hereinafter be referred to as *Time-varying h_l DNS* or $h_l = f(t,z)$ *DNS*. This information is synthesized in Table 1 for future reference.

Both cases focus on one of the reference geometries of the KIT-ITS test rig (Gepperth et al., 2010), whose parameters are summarized in Table 2. Even though the fuel is injected through an array of discrete holes distributed along the span on the prefilmer upper surface, it results in a totally wetted prefilmer for all the operating conditions experimentally reported in the literature, with an effective prefilming length L_f.

Both studied cases are investigated for the operating condition detailed in Table 3, corresponding to the test rig operated at atmospheric conditions. The reason for the choice of this condition, representative of altitude relight (Mosbach et al., 2010), is that it has been extensively studied in the literature both experimentally (Gepperth et al., 2010, 2012; Chaussonnet et al., 2018; Holz et al., 2018) and numerically (Mukundan et al., 2019a; Braun et al., 2019; Warncke et al., 2017, 2019; Carmona et al., 2021; Mukundan et al., 2019b,

Table 3
Functional parameters of the studied operating condition.

Description	Parameter	Value	Units
Temperature	T	298	K
Pressure	p	1	atm
Gas bulk velocity	$\bar{u}_g$	50	m/s
Gas density	ρ_g	1.21	kg/m^3
Gas dynamic viscosity	μ_g	1.82×10^{-5}	Pa s
Liquid normalized volumetric flow rate	$\dot{V}/b$	50	mm^2/s
Liquid density	ρ_l	770	kg/m^3
Liquid dynamic viscosity	μ_l	1.56×10^{-3}	Pa s
Liquid surface tension	σ	0.0275	kg/s^2
Gas Reynolds number	Re_g	13480	–
Liquid Reynolds number	Re_l	24.63	–
Weber number (traditional)	We_l	8.6	–
Weber number (based on atomizing edge)	We_h	25.3	–
Weber number (based on boundary layer)	We_δ	151.5	–
Ohnesorge number	Oh	0.0223	–
Density ratio	r	636.36	–
Momentum flux ratio	M	15.71	–

2022). Hence, a large database is consolidated and readily available to validate the developed numerical methodology.

Air is used as a gas in this operating condition, whereas the liquid is Shellsol D70. This liquid was chosen in the experiments to replicate the properties of kerosene or Jet A-1 at engine-like operating conditions. The relevant non-dimensional groups detailed in Table 3 are estimated as follows. The Reynolds numbers Re for each phase are calculated according to Eq. (1):

$$Re_g = \frac{\rho_g\, \bar{u}_g\, h_c/2}{\mu_g} \quad \text{and} \quad Re_l = \frac{\rho_l\, \dot{V}/b}{\mu_l} \tag{1}$$

where it can be seen that the half-channel width is chosen as the reference length for Re_g and the average liquid film thickness is used for Re_l from the volumetric flow rate or film loading $\dot{V}/b$.

As far as the Weber numbers are concerned, their definitions are in Eq. (2):

$$We_l = \frac{\rho_g\, \left(\bar{u}_g - \bar{u}_l\right)^2\, h_l}{\sigma} \quad We_{hp} = \frac{\rho_g\, \bar{u}_g^2\, h_p}{\sigma} \quad \text{and} \quad We_\delta = \frac{\rho_g\, \bar{u}_g^2\, \delta_{TE}}{\sigma} \tag{2}$$

where the main differences among definitions come from the characteristic dimension considered. For We_l, h_l is estimated from the volumetric flow rate and later verified in the computed 2-phase LES. The interest of We_{hp} resides in the fact that Chaussonnet et al. found that the SMD in part scales with $1/\sqrt{We_{hp}}$ (Chaussonnet et al., 2016). On the other hand, We_δ is based on the boundary layer thickness at the prefilmer trailing edge δ_{TE}, which is in turn estimated according to Eq. (3) by analogy to a turbulent boundary layer on a flat plate (White, 2006):

$$\delta_{TE} = 0.16\, \frac{L_p}{Re_{L_p}^{1/7}} \tag{3}$$

where Re_{L_p} is a specific gaseous Re based on the prefilmer length as the relevant dimension, which takes a value of 158,230 for the operating condition tested.

The Ohnesorge number Oh, in turn, is defined according to Eq. (4):

$$Oh = \frac{\mu_l}{\sqrt{\rho_l\, \sigma\, h_p}} \tag{4}$$

Finally, the momentum flux ratio is introduced in Eq. (5). Please note that the density ratio has been inversely defined as $r = \rho_l/\rho_g$ for illustrating purposes.

$$M = \frac{\rho_g\, U_g^2}{\rho_l\, U_l^2} \tag{5}$$

It is important to note that the proposed methodology implies taking the assumption that the flow in each region represented by a simulation is one-way coupled. This means that the simulations downstream are influenced by the upstream simulations, but not vice versa. This hypothesis constitutes a limitation of the study, as discussed next.

Fuster et al. (2013) studied the interfacial instability generated by a splitter plate among planar air–water coflowing sheets, in a configuration similar to the planar airblast atomizer from the present investigation. They investigated the transition between the two interfacial instability regimes, namely convective (in which the instability does not influence the flow upstream of the instability source) and absolute (in which the instability does influence the flow upstream of the instability source). In their study, Fuster et al. found the threshold between regimes to be governed by the dynamic pressure ratio and the density ratio. In particular, for a density ratio $r = 10$ the study reports a critical momentum flux ratio $M = 8$ above which the interfacial instability is absolute, but this value decreases to $M = 1$ for $r = 1000$. From here, it follows that the operating condition analyzed in the present study (Table 3) is deemed to trigger an absolute instability.

Consequently, through one-way coupling among simulations, the methodology proposed in the present investigation neglects the influence of the simulations of the downstream regions on the simulations of their upstream regions, even though there is a theoretical influence of the interfacial instability (triggered in the DNS domain of the present study) on the film flow (mainly computed in the two-phase precursor LES). The DNS domain will then include part of the prefilmer surface upstream of its edge, so that at least the film in this region is influenced by the interfacial instability. In any case, the comparison of the spatiotemporal film thickness evolution from the two-phase precursor LES (Section 4.1.2) against available experimental data will show the extent of validation of the methodology from a practical standpoint. A detailed analysis on the influence of the interfacial instability on the upstream flow would require a computation with the complete atomizer geometry, which is beyond the scope of the present investigation.

3. Computational methodology

The present section covers the details of the numerical simulations needed to complete the computational workflows depicted in Fig. 2 and Table 1. Hence, it presents the governing equations, meshing strategy and computational setup for each of the precursor LES needed to generate reliable data for the embedded DNS of the atomizing edge and for the DNS itself. The methodology used to post-process both the ligament arrangement and the droplet cloud predicted by the DNS are also explained in this section.

3.1. Precursor single-phase flow LES

3.1.1. Governing equations and related submodels

To solve the transient incompressible and turbulent channel flow along the planar prefilmer duct, the Pressure-Implicit with Splitting of
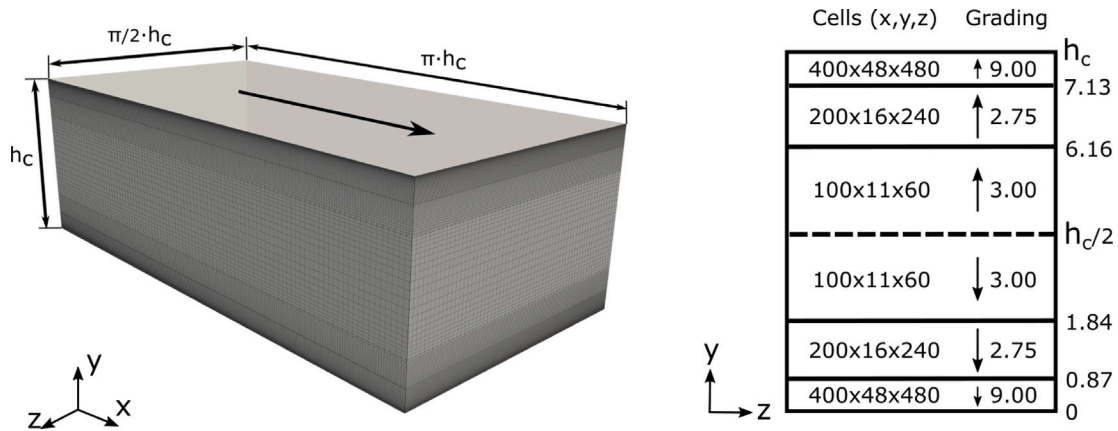
Fig. 3. Geometry and mesh sketch for the single-phase turbulent channel flow LES (left), detail of the number of cells and cell grading in each of the mesh zones (right).

Operators (PISO) algorithm (Issa, 1986) is used through the *pisoFoam* solver in the OpenFOAM open source CFD toolbox (Weller et al., 1998). It solves Eqs. (6) and (7) as the filtered governing equations for continuity and momentum conservation, respectively:

$$\nabla \cdot \bar{\mathbf{u}} = 0 \qquad (6)$$

$$\frac{\partial \bar{\mathbf{u}}}{\partial t} + \nabla \cdot (\bar{\mathbf{u}}\bar{\mathbf{u}}) = -\frac{1}{\rho}\nabla \bar{P} + \nabla \cdot \left[\left(\nu + \nu_{SGS}\right)\nabla \bar{\mathbf{u}}\right] \qquad (7)$$

Closure on the filtered governing equations is achieved through the subgrid scale viscosity ν_{SGS}, which is modeled by the Wall Adapting Local Eddy-viscosity (WALE) sub-grid scale (SGS) model from Nicoud and Ducros (1999).

3.1.2. Computational domain and mesh

Fig. 3 shows the geometrical dimensions of the computational domain and the mesh for the turbulent channel. The domain height in the wall-normal y direction replicates the full prefilmer channel height from the KIT-ITS test rig, h_c. The width in the spanwise z direction is chosen as $\pi/2 \cdot h_c$, according to Moser et al. (1999). The domain length in the streamwise x direction is $\pi \cdot h_c$, even though a periodic boundary condition is set in the streamwise edges in order to virtually mimic an infinitely long channel.

A zonal mesh strategy with hexahedral cells is adopted as in the work by Sauer et al. (2016). Fig. 3 (left) shows the geometry of the domain and the direction of the flow. The grid spacing is uniform in the streamwise and spanwise directions for every mesh zone, but a symmetric cell-size grading is applied in the wall-normal y direction to refine the domain from the channel core to the walls. Fig. 3 (right) presents the number of cells and a grading coefficient for all the 3 zones. This grading coefficient g_c is the proportion between the sizes of the first and last cell in that zone, following the arrow direction: $g_c = \frac{cell_0}{cell_N}$. The intermediate cell size increases or decreases linearly. A $y^+ < 1$ condition is fulfilled at the walls, preventing the use of wall functions. This strategy yields a total of 20.1 M cells.

3.1.3. Boundary conditions, discretization schemes and solution control

As far as the boundary conditions are concerned, gas velocity is initially prescribed at the inlet (X- boundary) by a Dirichlet boundary condition with $\bar{u}_g = 50\,\text{m/s}$ according to Table 3 and null values for v and w; whereas a Neumann boundary condition is used at the outlet (X+ boundary). A no-slip condition is used at the bottom and top walls (Y- and Y+ boundaries) and a periodic condition is used spanwise (Z- and Z+ boundaries). The *boxTurb* tool from OpenFOAM is used to initially trigger turbulence in the domain. It generates a divergence-free random initial velocity field consistent with the mesh. After a transient, both the inlet and outlet boundaries (X- and X+) are also converted into periodic boundary conditions. This configuration mimics

an infinitely long turbulent channel where turbulence can develop to simulate the prefilmer channel and may be passed on to the subsequent simulations according to Fig. 2 workflow. As long as the simulation is run for enough time in this virtually infinite configuration, the resultant turbulent velocity field is independent from the initialization from the synthetic turbulence generator, which only aids in speeding-up the process.

In order to map velocity data from this simulation to the subsequent ones, velocity data are sampled at the central YZ plane of the domain every 1 μs. It must be noted that the resultant turbulent channel flow simulation corresponds to $Re_\tau \approx 685$.

All chosen discretization schemes are 2nd order in time and space. As far as time discretization is concerned, a backward scheme (also known as 2nd order upwind Euler scheme (Lee, 2017)) is used, which replaces the time derivative of a flow property ϕ as given by Eq. (8):

$$\frac{\partial \phi}{\partial t} \rightarrow \frac{3\phi - 4\phi_{t-1} + \phi_{t-2}}{2\Delta t} \qquad (8)$$

Space discretization is needed for the divergence, laplacian and gradient operators of the convective, diffusive and pressure terms of Eq. (7), respectively. In this regard, OpenFOAM's FVM (Finite Volume Method) makes use of the Gauss theorem to convert cell-based volume integrals of a field divergence to surface integrals of the related vector field over the volume surface (i.e. flux across cell faces). Since flow properties are stored at the cell centroids after each time step in a collocated arrangement, the advection of a flow property ϕ requires the computation of cell face fluxes, for which interpolation from adjacent cell centroids is required. Linear interpolation of ϕ to the cell faces is chosen in what is known as a *Gauss linear* 2nd order scheme. Laplacian discretization also requires the computation of surface-normal gradients at cell faces. The surface normal gradients of a property ϕ are also computed by linear interpolation of the property from cell centroids to the cell faces, normalized by the distance among cell centroids. The same procedure is used for the discretization of the pressure gradient term. It must be noted that during the PISO loop for pressure–velocity coupling, the calculations are done with pressure at the cell centroids and the velocity components being interpolated at cell faces to compute the flux across them, thus in a staggered fashion. For further details on OpenFOAM's predefined discretization schemes, the reader is referred to Greenshields and Weller (2022).

Finally, a Geometric Agglomerated Algebraic Multi-Grid (GAMG) is used as the linear solver. The time step is let to vary during simulation runtime, being set by restricting the maximum CFL number to 0.6. This results in time steps in the order of 1×10^{-7} s.
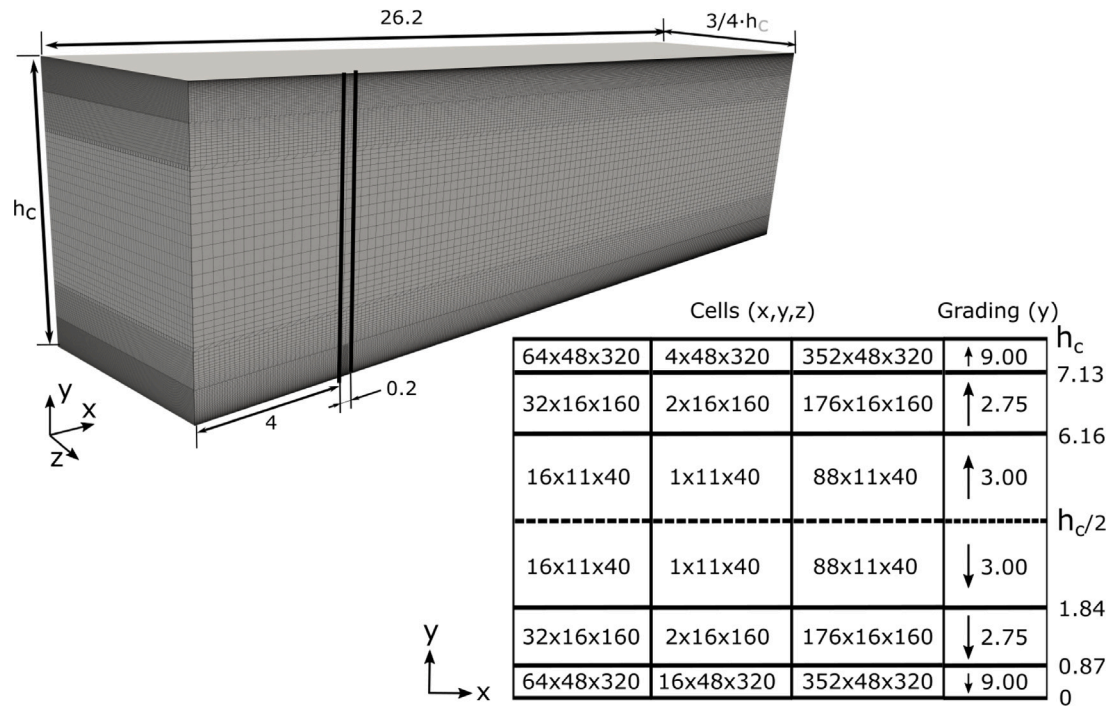
Fig. 4. Geometry and mesh sketch for the two-phase turbulent channel flow LES.

3.2. Precursor two-phase flow LES

3.2.1. Governing equations and related submodels

In order to solve the transient two-phase flow the *interFoam* solver within OpenFOAM is used. It applies the Volume of Fluid (VOF) interface capturing approach, which introduces the cell liquid volume fraction $\alpha = V_l/V_{cell}$ as a variable and advects it according to Eq. (9).

$$\frac{\partial \bar{\alpha}}{\partial t} + \bar{\mathbf{u}} \cdot \nabla \bar{\alpha} + \mathbf{u_c} \cdot \nabla \left[\bar{\alpha} \left(1 - \bar{\alpha} \right) \right] = 0 \qquad (9)$$

Eq. (9) is derived combining the separate mass conservation equations for both phases, under the assumptions that both of them are incompressible, isothermal and immiscible. Hence, the consideration is made that the flow velocity normal to the interface is zero. The last term in Eq. (9) is an artificial compression term that only acts in the vicinity of the interface (i.e. it is different than zero only when $0 < \alpha < 1$), creating a flux that counters numerical diffusion keeping a sharp interface (Wardle and Weller, 2013). The velocity vector $\mathbf{u_c}$ is defined according to Eq. (10):

$$\mathbf{u_c} = C_\alpha \left| \mathbf{u} \right| \mathbf{n} \qquad (10)$$

where C_α is a binary coefficient that switches interface sharpening on (with a value of 1) or off (with a value of 0), whereas $\mathbf{n}$ is the interface unit normal vector, used to define the direction of the applied compression velocity and approximated by Eq. (11):

$$\mathbf{n} = \frac{\nabla \alpha}{\left| \nabla \alpha \right|} \qquad (11)$$

In this work, C_α has been set as 1 so that interface sharpening is active. Additionally, surface tension is modeled through the Continuum Surface Force (CSF) model (Brackbill et al., 1992). A surface tension force $\mathbf{f}_\sigma$ is then included (correspondingly divided by ρ) as a source term in the momentum Eq. (7), depending on the surface tension σ and the interface curvature κ:

$$\mathbf{f}_\sigma = \sigma \kappa \delta_S \mathbf{n} \qquad (12)$$

where δ_S is a Dirac delta function that concentrates the effects of the surface tension on the liquid interface only and the curvature is approximated through Eq. (13):

$$\kappa = -\nabla \cdot \mathbf{n} \qquad (13)$$

The interface unit normal vector in Eq. (12) and (13) is again approximated through Eq. (11).

The density ρ and viscosity μ at a cell used in the continuity and momentum conservation equations are linear expressions of the fluid properties weighted by α.

$$\begin{aligned} \rho &= \alpha \rho_l + (1-\alpha)\rho_g \\ \mu &= \alpha \mu_l + (1-\alpha)\mu_g \end{aligned} \qquad (14)$$

Last, the WALE SGS model is again used to model sub-grid turbulence. Since this model was originally conceived for single-phase flow, this does not allow for a full modeling of the subgrid terms arising from the two-phase flow filtered equations, thus being a source for uncertainty. Noteworthy advances have been performed by the scientific community developing such models specific for two-phase flows (Aniszewski et al., 2012; Herrmann, 2013; Jofre et al., 2020), but they have not yet been benchmarked in practical engineering flows applications. Future works should count on these specific submodels to increase the reliability of the predictions.

3.2.2. Computational domain and mesh

Fig. 4 shows the geometry considered for the computational domain of the two-phase channel flow, together with the mesh used. The domain dimensions keep the full channel height h_c in the wall-normal y direction. In the streamwise x direction, there is enough space from the fuel inlet (included at the bottom of the domain) to the domain outlet for the film to develop half of the prefilmer effective film length L_f. Including some space to separate the fuel inlet from the air inlet, this yields a total length of 26.2 mm. Since the mesh in this case is finer than the one for the single-phase flow precursor LES, the width in the spanwise z direction is chosen as $3/4 \cdot h_c$ (nearly half of the single-phase flow precursor LES) in order to keep a limited amount of computational resources.

A zonal mesh strategy is utilized again. A cell-size grading is prescribed in the wall-normal y direction, similar to the one used in the single-phase flow precursor LES. In this case, however, an additional refined zone is added at the lower part of the domain in order to better
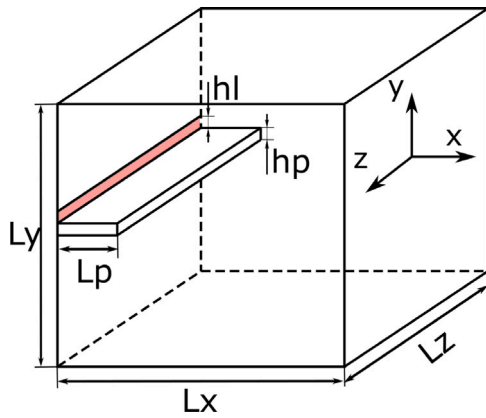
Fig. 5. Atomizing edge DNS computational domain. Flow direction is X^+ (from left to right).

Table 4
Main dimensions of the atomizing edge DNS computational domain.

Description	Parameter	Value [mm]
Domain length	L_x	6.08
Domain height	L_y	6.08
Domain span	L_z	4.00
Prefilming length	L_p	1.00

represent the gas–liquid interface. This yields a 4-step sequence from the wall-normal domain center to the bottom, keeping the condition of $y^+ < 0.9$ at the top and bottom walls, again preventing the use of wall functions. A local refinement is added at the streamwise location where the fuel inlet is placed. The grid spacing is uniform in the spanwise direction, but a slight grading is applied streamwise towards the outlet. This strategy yields a total cell count of 21.4 M cells.

3.2.3. Boundary conditions, discretization schemes and solution control

Air velocity is provided at the gas inlet (X- boundary) as a Dirichlet boundary condition with time-varying data mapped from the single-phase LES simulation, linearly interpolating among sampled planes. The fuel inlet at the Y- boundary occupies part of the streamwise direction and is uniformly distributed spanwise, so as to replicate the uniform fuel injection achieved upstream of the prefilmer edge at all operating conditions in the KIT-ITS test rig. A Dirichlet boundary condition is also used, liquid velocity being imposed according to the inlet area in order to prescribe the flow rate from Table 3. A Neumann boundary condition is used at the domain outlet (X+ boundary). A no-slip condition is used at the bottom (except for the fuel inlet region) and top walls (Y- and Y+ boundaries) and a periodic condition is again used spanwise (Z- and Z+ boundaries).

This configuration mimics the upper part of the KIT-ITS planar prefilmer so both the liquid film waves and the air-fuel boundary layer may be passed on to the subsequent atomizing edge DNS according to Fig. 2 (right) workflow. To this end, velocity and liquid volume fraction data are sampled at a YZ plane close to the domain outlet every 2 µs.

The pressure–velocity coupling is again solved using the PISO algorithm. The Multidimensional Universal Limiter for Explicit Solution (MULES) method within *interFoam* is used to solve for the liquid volume fraction advection given by Eq. (9). This method uses a Flux-Corrected Transport (FCT) algorithm (Zalesak, 1979) and in this work ensures the boundedness of the solution thanks to a predictor–corrector procedure. As it happened for the single-phase precursor LES, the chosen discretization schemes are 2nd order in time and space. The Crank–Nicolson method (Crank and Nicolson, 1947) is now used for the temporal discretization of α in Eq. (9), whereas the vanLeer scheme (van Leer, 1974) is chosen for the MULES limiter. The fully discretized version of Eq. (9) using MULES and the description of the predictor–corrector procedure used in this investigation are given by Kim et al. (2019). The discretized version of the momentum equation using *interFoam* is given by Deshpande et al. (2012).

The Geometric Agglomerated Algebraic Multi-Grid (GAMG) is again used as the linear solver. A fixed time step of 5×10^{-8} s is used in this case, ensuring the maximum CFL number never surpasses 0.25. The resulting time steps are also checked to comply with additional criteria

for capillary velocity and viscosity constraints in order to reduce the growth of spurious currents as stated by Deshpande et al. (2012), even though they state this phenomenon not to be a major issue for inertia-dominated flows.

It must be noted that the chosen interface compression and curvature evaluation methods are in general not as physically accurate as interface reconstruction methods (such as PLIC) and other curvature approaches (such as the use of Height Functions or hybridization with the Level Set method). However, it must be considered that the precursor two-phase flow LES does not look at solving for liquid atomization, but for the inertia-dominated free-surface flow, where the exact reproduction of curvature is not deemed to be critical. Hence, the fact that the chosen method is mass conservative (Wardle and Weller, 2013) is the reason for its choice towards coupling with the two-phase flow DNS. This approach for the VOF method and curvature handling has been successfully validated elsewhere for two-phase wave simulation with an orthogonal mesh (Kim et al., 2019).

3.3. Atomizing edge two-phase flow DNS

3.3.1. Governing equations and related submodels

To solve the incompressible, isothermal and immiscible two-phase flow at the atomizing edge with a Direct Numerical Simulation (DNS) approach, the PARIS (PArallel, Robust, Interface Simulator) code (Aniszewski et al., 2021) is used. It applies the Navier–Stokes equations in the one-fluid formulation of two-phase flow, including also the Continuum Surface Force (CSF) method to compute surface tension forces:

$$\rho \left[\frac{\partial \mathbf{u}}{\partial t} + \nabla \cdot (\mathbf{uu}) \right] = -\nabla p + \mu \nabla^2 \mathbf{u} + \sigma \kappa \, \delta_S \, \mathbf{n} \tag{15}$$

The VOF method is used to capture the interface according to Eq. (16), computing density and viscosity as in Eq. (14).

$$\frac{\partial \alpha}{\partial t} + \mathbf{u} \cdot \nabla \alpha = 0 \tag{16}$$

Please note the differences in VOF advection with the two-phase precursor LES. In this case, a modified Piecewise Linear Interface Capturing (PLIC) approach called CIAM (Li, 1995) is used to reconstruct the interface and to compute its unit normal vector $\mathbf{n}$ (Scardovelli and Zaleski, 2003) for the CSF. The curvature κ is estimated from the Height Function (HF) method proposed by Popinet (2009) and whose full implementation details in PARIS are described by Aniszewski et al. (2021). For these reasons, Eq. (16) leaves aside the artificial interface compression term introduced in Eq. (9).

3.3.2. Computational domain and mesh

The geometry of the atomizing edge DNS domain is showed in Fig. 5. The illustrated domain dimensions are compiled in Table 4. These dimensions are very similar to the ones used in comparable computations in the literature (Mukundan et al., 2019a; Sauer et al., 2014; Warncke et al., 2017; Mukundan et al., 2019b, 2022). Including a prefilming length (L_p), rather than directly mapping the data from the precursor simulations at the prefilming edge axial location, allows the film to evolve on the prefilmer surface accounting (to a limited extent) for the absolute nature of the interfacial instability.. Additionally, the prefilmer edge thickness h_p was shown in Table 2. As per the liquid film thickness, the value $h_l = 0.08$ mm is used in the $h_l \neq f(t, z)$ case
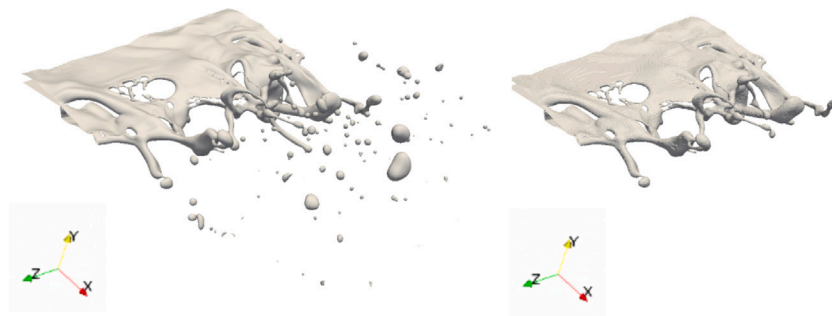
Fig. 6. All liquid structures identified in the domain through an iso-surface of $\alpha = 0.5$ (left), liquid core extracted through the connectivity algorithm (right). Images correspond to a given instant of the $h_l = f(t, z)$ case.

(corresponding to the rounded value obtained in the precursor two-phase LES), whereas it fluctuates in the $h_l = f(t, z)$ case as stated in Table 1, this being the object of investigation.

A staggered Cartesian grid is used in this case, with pressure collocated at the cell centres and velocities located at the face centres. The calculated Re yields a Kolmogorov length scale $l_\eta = 12\,\mu m$, implying a minimum grid spacing of $\Delta x_{min} = 25\,\mu m$ according to Pope's criterion (Pope, 2000). A cell size $\Delta x = \Delta y = \Delta z = 10\,\mu m$ is chosen for both cases, resulting in 147.87 million cells. This resolution matches the one by Warncke et al. (2017), who already justified that Sauer et al. (2016) had performed a detailed discussion about the droplet representation with different grid sizes ($20\,\mu m$ and $10\,\mu m$). They found that a resolution of the entire liquid mass is hardly achievable, but that the $10\,\mu m$ cell size allowed a resolution of 80% of the liquid mass.

3.3.3. Boundary conditions, discretization schemes and solution control

A Dirichlet boundary condition is provided at the inlet (X- boundary), with time-varying velocity data mapped from the precursor LES in the $h_l \neq f(t, z)$ case, and both time-varying velocity and liquid volume fraction α in the $h_l = f(t, z)$ case. Linear interpolations among temporally sampled planes are used in both cases. A special convective and time-varying boundary is used in the outlet (X+ boundary) to reduce reflections (Kajishima and Taira, 2017), as expressed in Eq. (17), where u_m is computed at each time step as the average streamwise velocity at the inlet.

$$\frac{\partial u_i}{\partial t} + u_m \frac{\partial u_i}{\partial x} = 0 \tag{17}$$

For the bottom and top bounds (Y- and Y+ boundaries) a slip boundary condition (i.e. moving wall) is used with a streamwise velocity equal to the mean gas velocity. This condition allowed containing major flow vortices, with the chosen L_y dimension ensuring no influence on the region of interest for primary atomization. A periodic condition is used spanwise (Z- and Z+ boundaries).

Last, a no-slip boundary condition is used for the immersed boundary (prefilmer solid wall). A static contact angle among the prefilmer solid wall and the liquid has been introduced as a VOF condition to account for wettability. As formulated by Lacis et al. (2022) following Legendre & Maglio's work (Legendre and Maglio, 2015), this boundary condition is mathematically set by defining the interface normal unit vector at the boundary (**n**) through Eq. (18) wherever the interface is attached to the prefilmer wall:

$$\mathbf{n} \cdot \mathbf{n_{wall}} = \cos(\theta) \tag{18}$$

where $\mathbf{n_{wall}}$ is the wall-normal unit vector. A contact angle $\theta = 60°$ has been set between the liquid and the prefilmer according to Braun et al. (2019).

The spatial and time discretization schemes are 2nd order, using a multigrid solver with a V-cycle to solve the Poisson equation. In the case of temporal discretization, a predictor–corrector method is used, with an explicit projection step for the pressure. A complete description

of the methods is given elsewhere (Aniszewski et al., 2021; Tryggvason et al., 2011). A variable time step is used (limited to a maximum of 2×10^{-8} s), ensuring the maximum CFL number never surpasses 0.2. Computations are run with 4096 CPU cores for a total simulated time of about 9 ms, so that 3 main breakup events are accounted for in both cases (a first event is discarded, as it corresponds to a simulation transient). This required 0.21M core-hours per each millisecond of simulated physical time.

3.3.4. Post-processing

Different post-processing tools have been implemented and applied to the atomizing edge DNS data in order to generate and analyze quantitative results.

The first step to post-process the DNS data is to identify each individual continuous liquid structure. This is done scanning the whole domain looking for free surfaces according to an α threshold. Fig. 6 (left) shows a visualization of the instantaneous liquid–gas interface through an iso-contour of $\alpha = 0.5$ (value used as a threshold in the present investigation). After a binarization using that threshold, the connectivity algorithm from The Visualization Toolkit (VTK) (Schroeder et al., 2018) is applied to the domain for all time steps in order to identify every isolated liquid structure, obtaining their position and size. Once this is achieved, the intact core is identified as the first structure (including the film and any ligament directly attached to it, as shown in Fig. 6 -right) and separated from the droplet cloud and any detached ligaments. This way, the intact core and ligaments can be independently processed on the one hand, whereas the droplet characteristics can be analyzed on the other hand.

Intact core and ligament analysis

As far as the ligaments are concerned, it must be noted that experimental results available in the literature provide 2D shadowgraphy images (Gepperth et al., 2012; Chaussonnet et al., 2020; Warncke et al., 2017). Hence, as a first approach, the liquid data from the DNS is projected on the XZ plane in order to obtain comparable images for validation purposes.

The liquid projection is obtained by aggregating the values of the α variable along the Y axis at each XZ plane location. The resulting data is binarized with a chosen threshold ($\alpha = 1$), yielding images such as the one labeled as Step 1 in Fig. 7. Then, the isolated ligaments must be extracted from the intact core or liquid film. The method proposed to this end is as follows. For each Z coordinate, a function expressing the number of liquid cells before the first gas cell along the X axis is computed (Fig. 7 Step 2). Next, big slopes are detected with the derivative of this function and erased with a cutting and smoothing algorithm, obtaining the main liquid core except for the elongated structures (Fig. 7 Step 3). This structure is then used as a cutting mask, substracting it from the projected domain from Step 1 and obtaining the ligaments as isolated structures, noise being removed by deleting structures with very small areas (Fig. 7 Step 4). Finally, each ligament is labeled using the connectivity algorithm from OpenCV (Bradski, 2000).
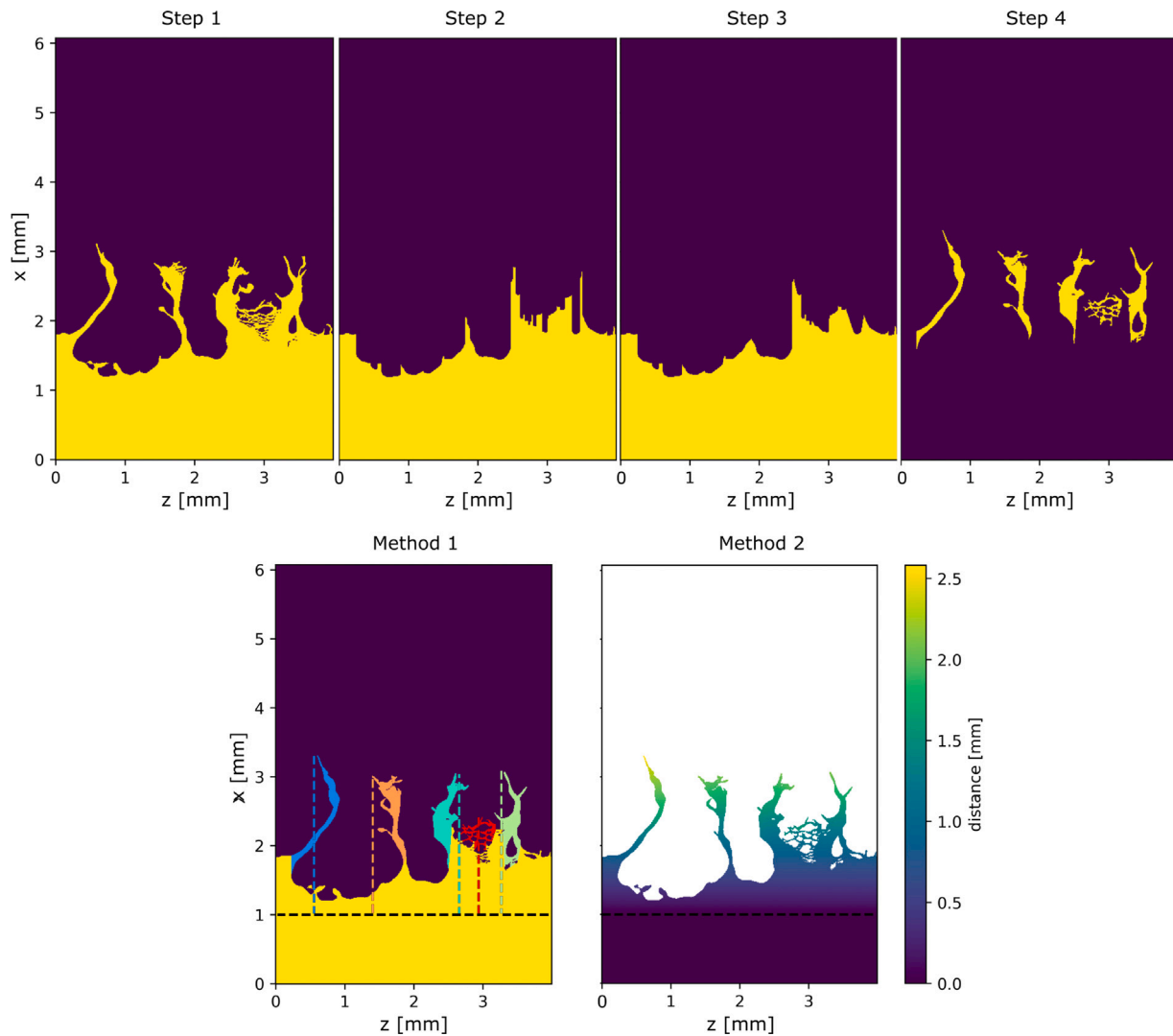
Fig. 7. Steps for 2D ligament analysis (top): liquid core and ligaments projected over the XZ plane and binarized (Step 1), mask construction (Steps 2 and 3) and isolated ligaments obtained (Step 4). Methods for ligament length measurement (bottom): Axial distance method (Method 1) and Fast Marching Method (Method 2). Images correspond to a given instant of the $h_i \neq f(t,z)$ case.

Once a ligament is characterized, the cell with the maximum X coordinate is considered to be the tip of that ligament. With that information, there are two methods for measuring string length $L_{str2D,i}$ as shown in Fig. 7 (bottom). Method 1 (left) considers the ligament length as the axial distance among the prefilmer edge and the ligament tip, following a straight line in the X direction. This is the simplest method and is also used in the literature shadowgraphy experiments and the simulations by Warncke et al. (2017). Hence, it has been used to validate the computations of the present work. Method 2 (right), proposed in this study, uses the *distance* function of the *scikit-fmm* package in Python, which is an implementation of the Fast Marching Method by Sethian et al. (Sethian, 1996) to solve an Eikonal equation. Defining the prefilmer edge as a propagating surface, and setting the same constant velocity for every node in the domain, it returns a distance matrix that is equivalent to the continuous shortest path along ligament connectivity points between the prefilmer edge and each ligament cell.

In this work, ligament length data are complemented with ligament velocity data. During the 2D ligament projection step, at each XZ plane location, liquid velocities are obtained by adding the values of velocity along the Y axis weighted by α. An example of the resulting velocity projected data for a given time step is shown in Fig. 8. Velocity data at the tip of each ligament i ($\mathbf{u_{str2D,i}}$) are obtained from this projection.

Besides, a characteristic streamwise velocity of the liquid film is also computed according to the procedure by Warncke et al. (2017). From the liquid volume projection (Fig. 7 Step 1) of a given time step t_k, the furthest location of the attached liquid ($x_{max,zk}$) is determined for each z position. The streamwise deformation velocity at each z location is directly computed among time steps t_k and t_{k-1} as $u_{def,zk} = (x_{max,zk} - x_{max,zk-1})/\Delta t$. The characteristic film deformation velocity of the t_k time step ($u_{def,k}$) is then defined by the 90% percentile of all $u_{def,zk}$ locations.

After 2D data for validation are obtained, a novel 3D methodology is proposed to prevent DNS information loss during the projection step. The objective is to preserve the 3D nature of the ligaments both in terms of ligament size and tip velocity components for a more realistic description of these structures. To this end, the cutting mask obtained in the 2D analysis is extruded along the Y axis so it can be used as a 3D cutting mask. When applied to the connected liquid in the domain, only the ligaments are left. It is then possible to apply another connectivity filter, identifying ligaments sizes and positions as depicted in Fig. 9. Properly locating ligaments and the film in the 3D domain in this way then allows processing string tips, string lengths $L_{str3D,i}$ with the Fast Marching Method (Method 2), and the velocities $\mathbf{u_{str3D,i}}$ directly from the DNS output data.
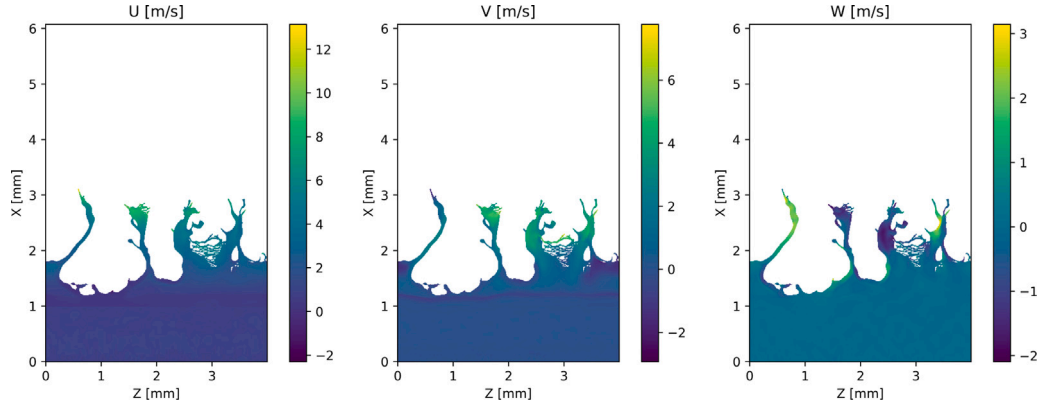
Fig. 8. Liquid core velocity components projected on the XZ plane for a given time step of the $h_l \neq f(t, z)$ case.
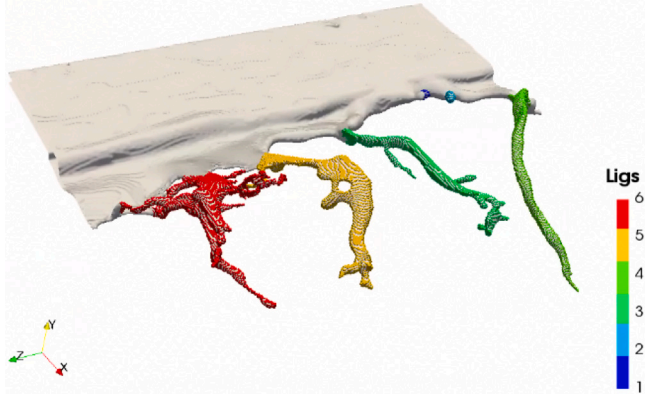

Fig. 9. Sample of ligament detection in the 3D domain for a given time step of the $h_l \neq f(t, z)$ case.

Regardless of the geometrical treatment given to the ligaments (2D and 3D), some additional quantities derived from their features can be used to globally characterize the breakup process. A global breakup length is defined by averaging ligament lengths for all time steps ($L_{bu} = \overline{L_{str}}$) and a mean ligament tip velocity can be computed by averaging ligament velocities for all time steps ($\mathbf{u_{lig}} = \overline{\mathbf{u_{str}}}$). Besides, a mean film deformation speed is also computed as the average among time steps ($u_{def} = \overline{u_{def,k}}$). From these quantities, a mean breakup frequency (f_{bu}) is estimated according to Eq. (19) (Warncke et al., 2017):

$$f_{bu} = \frac{u_{def}}{L_{bu}} \tag{19}$$

Finally, in the case of the 3D analysis, an equivalent diameter of each ligament can be defined from their determined length and volume according to Eq. (20):

$$d_{eq,i} = \frac{V_{lig,i}}{L_{str3D,i}} \tag{20}$$

Droplet cloud analysis

Focusing on the droplet cloud, it has been processed through the same method used by Crialesi-Esposito et al. and validated for a round spray (Crialesi-Esposito et al., 2022), which is here summarized. Each individual droplet i is assigned its volumetric diameter according to Eq. (21), taking the assumption of spherical droplets.

$$d_{V,i} = \sqrt[3]{\frac{6}{\pi} V_{drop,i}} \tag{21}$$

where the droplet i liquid volume ($V_{l,drop,i}$) is calculated as the sum of the liquid volume for every cell j belonging to the droplet, as given by Eq. (22):

$$V_{drop,i} = \sum_{j=1}^{Ncells} \alpha_j V_{cell,j} \tag{22}$$

where $Ncells$ is the number of cells representing droplet i. Droplet velocities are computed as weighted averages of the velocity from each cell j composing the droplet as shown in Eq. (23), using the liquid volume fraction as the weighing factor:

$$\mathbf{u_{drop,i}} = \frac{\sum_{j=1}^{Ncells} \alpha_j \cdot \mathbf{u_j}}{\sum_{j=1}^{Ncells} \alpha_j} \tag{23}$$

Any other droplet characteristics of interest (local Re, local We, etc.) can be computed from these magnitudes. Probability density function (PDF) graphs of both diameters and velocities are provided and analyzed in Section 4.2.2. Droplets with $d_v < 20\,\mu m$ are discarded from the analysis for two reasons: on the one hand, this is the smallest droplet size detected by the reference experiments used for validation (Warncke et al., 2017). On the other hand, this value corresponds to twice the cell size realized by the proposed VOF-DNS simulations.

4. Validation and results

Results of the methodology are presented in this Section. First, each of the precursor LES is independently validated against experimental data. Next, results from the atomizing edge DNS for the two computed cases are presented, both from a qualitative and a quantitative standpoint. Quantitative results are also compared to experimental data for validation purposes.

4.1. Validation of the precursor simulations

4.1.1. Single-phase flow LES

For illustrating purposes, Fig. 10 shows an example of the instantaneous data samples in a YZ plane mentioned in Section 3, where the spatial variability of each velocity component can be appreciated.

The velocities of these YZ planes are spatially averaged over the Z axis and temporally averaged for a large window in order to analyze the wall-normal velocity profile and whether it conforms with the law of the wall. Results for the mean dimensionless streamwise velocity profile are shown in Fig. 11 (left), where they are also compared to the theoretical law of the wall and to accepted turbulent channel flow DNS data by Iwamoto et al. (2002) for $Re_\tau \approx 650$. LES data show a reasonable agreement with the theoretical relations, with a smooth transition from the viscous sublayer to the log-law region. The agreement is comparable to that of a DNS computation, highlighting the level of resolution achieved by this precursor LES.

The root mean square (RMS) of each velocity component are similarly computed and averaged. Their wall-normal evolution is plotted against Iwamoto's DNS data in Fig. 11 with a similar level of agreement, although a slight underprediction is present for all components.

Additionally, the turbulence spectra were also analyzed through the autocorrelations of the velocity components to ensure sampled data correspond to a statistically steady time series and no artificially induced frequencies are passed on to subsequent simulations.
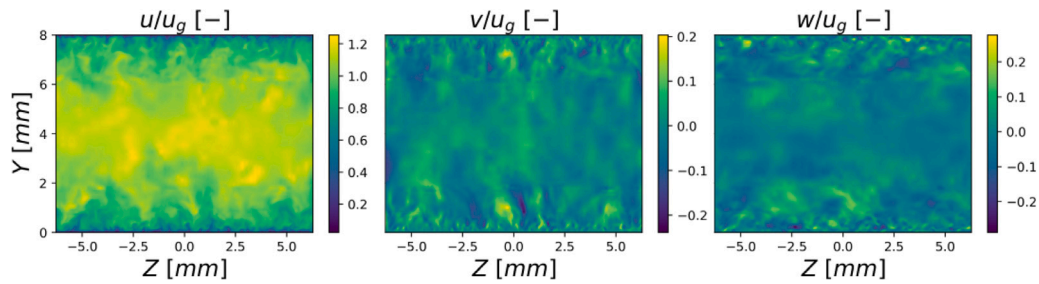
Fig. 10. Snapshots with the three normalized components of the velocity at $t = 2.5$ ms. Note the different scale in each case.
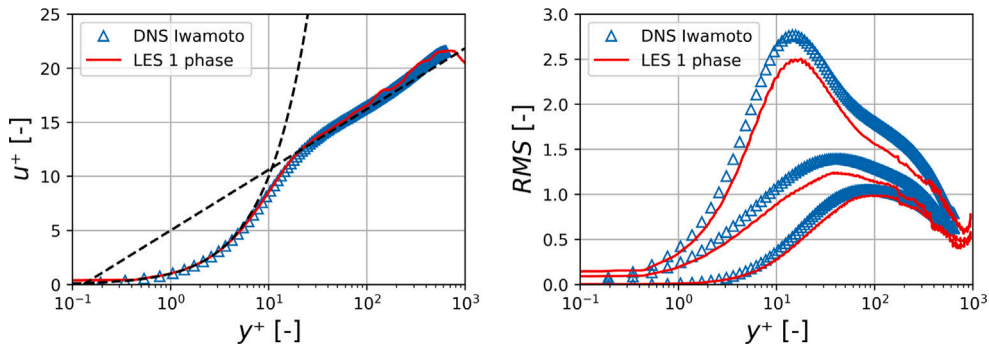

Fig. 11. Comparison of the single-phase LES temporally and spatially averaged velocity results against DNS data from Iwamoto et al. (2002): non-dimensional mean streamwise velocity profile (left, with the theoretical law of the wall sublayers also depicted in black), non-dimensional root mean square velocity components (right, from largest to lowest values: u^+, w^+, v^+).
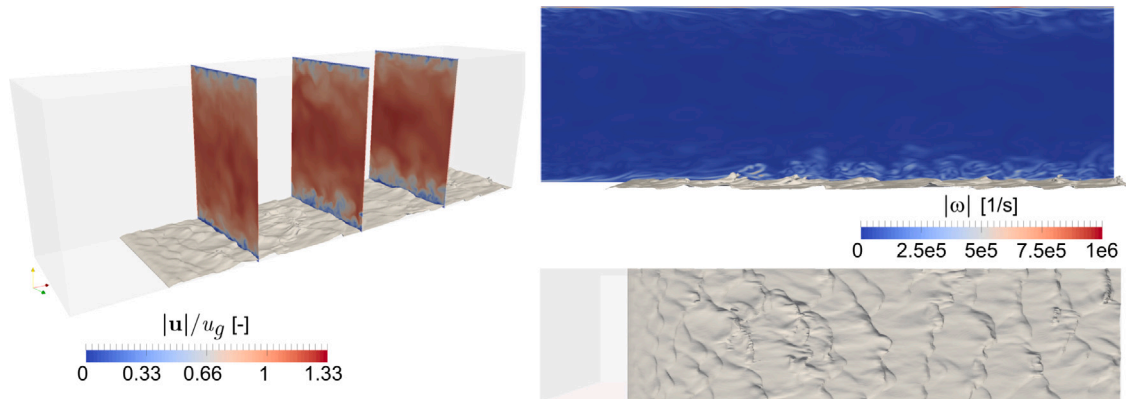
Fig. 12. Qualitative appearance of the liquid film on the prefilmer depicted through a $\alpha = 0.5$ iso-surface for a given time instant. 3D representation with velocity data at three different streamwise locations (left), side view with vorticity magnitude in a mid-plane (right, top), top view (right, bottom).

4.1.2. Two-phase flow LES

In the case of the two-phase flow LES, results were analyzed once the liquid injection transient was finished. Fig. 12 (left) shows the qualitative appearance of the film for a given instant. Normalized velocity data at three different YZ planes are shown to illustrate the influence of the liquid film on the gaseous phase velocity, as a liquid–gas boundary layer is developed. Fig. 12 (right, top) depicts a side view of the liquid film. Vorticity magnitude data at the mid XY plane is shown, where it may be seen how the liquid–gas interaction along the film crests and valleys generates additional vortex to the ones generated at the gas–wall boundary layer on the upper wall. These vortex also spread for a larger distance from the film in the wall-normal direction than they do in the case of the gas–wall interaction. This fact also highlights the generation of a thicker boundary layer among liquid and gas. A top view of the film is also shown in Fig. 12 (bottom) to complete the qualitative appearance of the liquid film, showing the wavy behavior with crests and valleys being shaped and propagated

in the streamwise direction. Several wave crests or valleys can be contained in the spanwise direction.

In this case, liquid volume fraction (α) data sampled at the three YZ planes and at the domain mid-plane (XZ) were processed to compute the liquid film height at all locations and their temporal evolution. The analysis allowed determining that data at the $x = 2 \cdot h_c$ location is already not influenced by the inlet boundaries and thus can be passed on to the atomizing edge DNS. The temporally averaged mean liquid film height and the corresponding standard deviation found at this location are plotted in Fig. 13 against experimental data for similar conditions reported by Gepperth et al. (2010). Further averaged results at this location are displayed in Table 5. It must be stated that the mean temporal frequency value obtained by the LES ($\overline{f_{film}} = 585.9$ Hz) is also very close to the one reported by Holz et al. (2018) ($\overline{f_{film}} = 595$ Hz) for the same operating condition. In order to extend the assessment of the validity of the two-phase flow LES, computational results for four additional operating conditions are also shown in Fig. 13 and Table 5, including additional gas velocities ($\bar{u}_g = 20$ m/s and $\bar{u}_g = 70$ m/s) and an

Table 5

Temporally averaged data for the 2-phase flow LES at $x = 2 \cdot h_c$ (target operating condition in bold, additional operating conditions are also reported).

Description	Parameter	Units	Shellsol D70			H$_2$0-1,2-Propanediol	
Liquid	–	–	Shellsol D70			H$_2$0-1,2-Propanediol	
Gas bulk velocity	$\bar{u}_g$	m/s	20	**50**	70	50	70
Mean film height	$\overline{h_l}$	µm	101.3	**74.3**	62.5	104.5	86.4
Film height std dev.	σ_{hl}	µm	–	**7.5**	7.1	8.1	7.8
Mean film wave freq.	$\overline{f_{film}}$	Hz	–	**585.9**	822.8	435.9	554.6
Mean film wavelength	$\overline{\lambda_{film}}$	mm	–	**2.28**	1.99	2.59	2.61
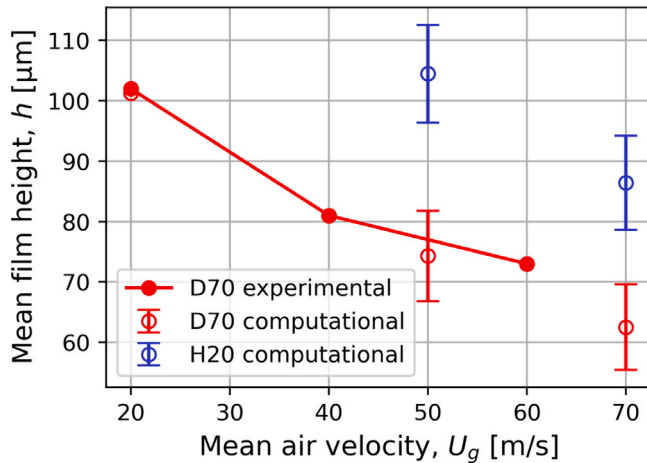
Fig. 13. Mean film height $\bar{h}_l$ as a function of the bulk gas velocity for the simulations and experimental data from Gepperth et al. (2010). Computational values, gathered for two different fluids, were obtained at $x = 2 \cdot h_c$ and also depict the standard deviation σ_{hl} (both temporally and spatially along the z axis) from the mean film height. Experimental data were reported for Shellsol D70 and the same normalized volumetric flow rate (Gepperth et al., 2010).

additional liquid (a H$_2$0-1,2-Propanediol mixture with $\rho_l = 1008\,\text{kg/m}^3$, $\mu_l = 6.06 \times 10^{-3}\,\text{Pa s}$ and $\sigma = 0.0466\,\text{kg/s}$). Computational results are thus compatible with available literature data. The model is sensitive to the variations in global inputs, as given by the expected trends: for a given fluid, mean film thickness decreases with the mean gas velocity; whereas for a given gas velocity, mean film thickness increases with increasing liquid density, viscosity and surface tension (i.e. decreasing We_l). The standard deviation with respect to the mean value is similar among moderate gas velocities cases (this value could not be reported for $\bar{u}_g = 20\,\text{m/s}$, as a long simulation time is needed to account for a statistically significant number of wave peaks). As far as the film wave frequencies are concerned, they increase with increasing gas velocity and decrease for the denser, more viscous fluid.

The predictions by this precursor 2-phase flow LES are successfully validated by these means, considering that the proposed methodology implies one-way coupling among simulations so that the effect of the interfacial instability generated by the prefilmer edge on the upstream flow is not accounted for. The averaged value of h_l is passed on to the $h_l \neq f(t,z)$ atomizing edge DNS, whereas sampled data are provided to the $h_l = f(t,z)$ case.

4.2. Two-phase flow DNS simulations

Results of the atomizing edge DNS are analyzed in the present Section. First, a qualitative analysis is carried out, describing the atomization mechanism and comparing its appearance for both tested strategies. Next, a quantitative analysis of the ligament development and the generated droplet cloud is carried out in Sections 4.2.1 and 4.2.2, respectively.

Fig. 14 illustrates the temporal evolution of the flow for a given breakup event of both simulated cases. To this end, it represents a series of snapshots depicting the evolution of the airblasted sheet. The liquid film and structures are characterized by iso-surfaces of $\alpha = 0.5$, as it is representative of the liquid–gas interface. Focusing on the $h_l \neq f(t,z)$ case on the one hand, the breakup mechanism phenomenology already described in the literature (Gepperth et al., 2012; Chaussonnet et al., 2020, 2016; Sauer et al., 2016; Warncke et al., 2017) is reproduced. First, the liquid transported along the prefilmer tends to accumulate behind the prefilmer edge, generating a liquid reservoir ($t = 2.46\,\text{ms}$). Two structures then emanate from this reservoir: elongated structures (ligaments) on the one hand, and most importantly a liquid sheet that tends to flap upwards or downwards. This liquid sheet then gets exposed to the free gas stream coming from above or below the prefilmer surface, shaping bag-like structures (observed at $t = 2.46\,\text{ms}$ and $t = 2.61\,\text{ms}$) that keep growing in size. Eventually, surface tension cannot keep the bag structures attached to the liquid sheet, so they get punctured and break into droplets in the so-called *bag breakup* ($t = 2.61\,\text{ms}$ and $t = 2.75\,\text{ms}$). Additionally, some rims are shaped from the sides of the bag structures ($t = 2.75\,\text{ms}$), generating separated ligaments that also break into droplets ($t = 2.91\,\text{ms}$). Some of these ligaments keep attached to the liquid film that starts generating a new reservoir behind the prefilmer edge. If these ligaments do not detach among main breakup events, they get thicker by receiving some liquid transported from the film (back to $t = 2.46\,\text{ms}$). Therefore, in the end, droplets are generated by two main mechanisms: bag breakup, which generates a large amount of small droplets only during the main breakup events; and ligament breakup, which generates a lower amount of relatively bigger droplets, some of them still being generated among breakup events. The coexistence of these distinct breakup mechanisms and the importance of the liquid accumulation process is justified considering the value of the momentum flux ratio ($M = 15.7$) achieved for this operating condition: Fernandez et al. (2009) found this value led to the so-called *torn sheet breakup*. According to these authors, values of $M > 20$ would have led to the *membrane sheet breakup*, with a low importance of the accumulation mechanism in favor of a direct disintegration in droplets behind the prefilmer edge; whereas $M < 5$ would have led to the *stretched ligament breakup*, with a higher presence of ligaments generated from rims after bag breakup.

On the other hand, a look at the $h_l = f(t,z)$ case highlights the qualitative differences when accounting for the liquid film history upstream of the prefilmer edge. In this case, the liquid film above the prefilmer surface appears more wrinkled than in the $h_l \neq f(t,z)$ case, as a consequence of the two-phase LES data mapping procedure. Therefore, the reservoir behind the prefilmer edge is less uniformly distributed spanwise than it was for the constant film thickness case, as the film crests and valleys do not reach the reservoir in a synchronized manner (recall Fig. 12). As a result, by the time a bag is formed and flapping, not the complete prefilmer span is filled with enough liquid to shape bags. Hence, while the breakup mechanism remains the same as in the $h_l \neq f(t,z)$ case, the aforementioned fact results in a less violent main bag breakup event. The amount of generated droplets is substantially lower, and the resulting cone-like injection zone is narrower in the $h_l = f(t,z)$ case than in the $h_l \neq f(t,z)$ case. Also, the shaped ligaments tend to be thicker, thus resulting in larger droplets from ligament breakup. In short, even though there are still main breakup events, the atomization seems inhibited to a certain extent, but seems more continuous in time.
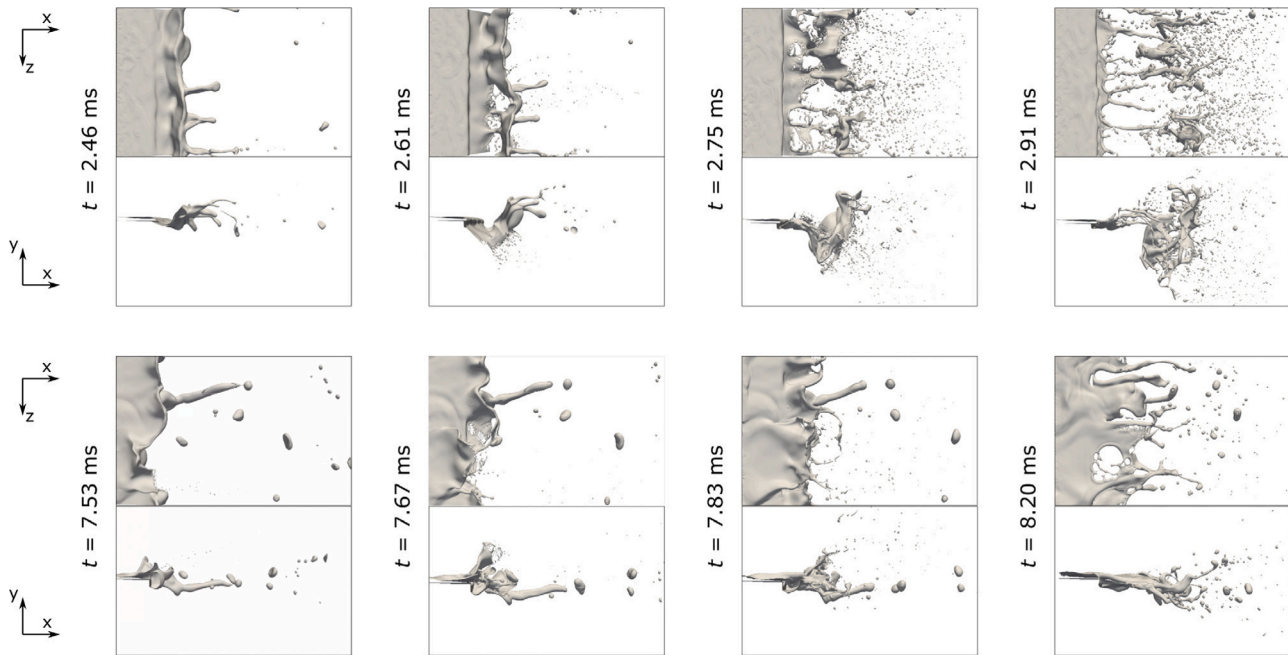
Fig. 14. Time sequence of the DNS results for the $h_l \neq f(t,z)$ case (top) and the $h_l = f(t,z)$ case (bottom). The liquid is depicted through an iso-surface of $\alpha = 0.5$.

4.2.1. Ligaments results

Ligaments are characterized in 2D through the liquid volume fraction α projection in the XZ plane and the identification of individual elongated structures, as detailed in Section 3.3.4. The histogram of ligament lengths is shown in Fig. 15 for both simulated cases and both experimental and DNS data from the literature. First, it must be mentioned that both ligament size distributions obtained by the DNS simulations presented in this investigation importantly differ from the experimental data reported in the literature. However, Warncke et al. (2017) already justified that the experiment occasionally reports several ligament lengths beyond the DNS domain ($L_{str} > 5\,\mathrm{mm}$), with a wide time window (i.e. a long amount of breakup events) being analyzed. In the simulations, no structure attached to the intact core was found to trespass the domain outlet, with maximum lengths around $L_{str} = 4\,\mathrm{mm}$. Reliably predicting the maximum ligament length for the operating condition studied would then imply enlarging the DNS domain and analyzing a greater amount of breakup events. Both actions are beyond the current affordable computational resources for a DNS study. In any case, the comparison of both $h_l \neq f(t,z)$ and $h_l = f(t,z)$ cases with the literature DNS (which uses the same domain length as the one used in the present study) shows fairly similar distributions, with ligament lengths spanning from 0 to $4.5\,\mathrm{mm}$ and most values being found among 1.5 and $2.5\,\mathrm{mm}$. An improvement in the predictions is found in the $h_l = f(t,z)$ case with respect to the $h_l \neq f(t,z)$ case, as the distribution as a whole and its mode are shifted towards longer lengths when the liquid film thickness evolution is accounted for at the DNS inlet. Besides, the distribution more closely resembles a normal distribution, as it was found for the experiments. The irregular shape from the distribution can be attributed to the fact that only 3 breakup events could be simulated.

Before analyzing the results found through the 3D post-processing strategy, it is interesting to assess the differences among Method 1 (axial distance method) and Method 2 (Fast Marching Method) for ligament length determination, since 3D sizes can only be determined through Method 2. Fig. 16 shows this comparison for the $h_l \neq f(t,z)$ and $h_l = f(t,z)$ cases. In both cases, the distributions found through both methods are relatively similar. Ligament sizes predicted through Method 2 are statistically slightly displaced towards larger values, as expected considering that the whole ligament path is computed as
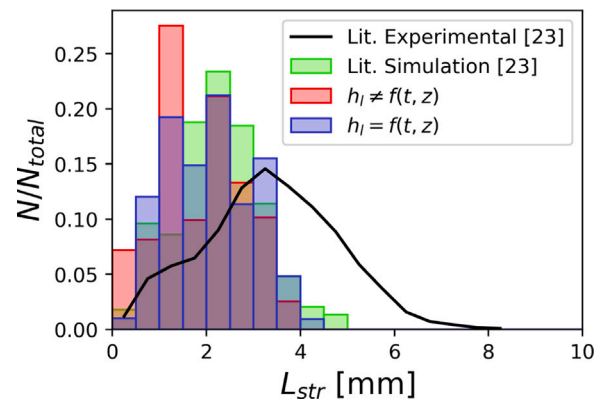

Fig. 15. Ligament 2D length distribution for both simulated test cases (Method 1 used for ligament length measurement). Literature DNS and literature experiments are also reported (Warncke et al., 2017).

opposed to only accounting for streamwise variations in the ligament tip location. Anyway, this method displays its potential for the 3D ligament detection case, for which it is strictly needed.

Once the differences among ligament length determination methods have been assessed, Fig. 17 depicts the results obtained in the ligament 3D lengths between simulated test cases. Focusing on one of the simulated test cases separately, a certain shift towards greater ligament lengths is observed compared to the analogous 2D distributions with Method 2 from Fig. 16, as logical. Except for the shortest ligaments (hardly distinguishable from the intact film), the $h_l \neq f(t,z)$ case more closely resembles a normal distribution. Despite the comparison in 2D (Fig. 15) showing longer ligament lengths for the $h_l = f(t,z)$ case, the 3D ligament length distribution found for the $h_l \neq f(t,z)$ case is more shifted towards greater values. Hence, these differences must be attributed to the more acute flapping observed when liquid accumulation behind the prefilmer edge is synchronized along the span, as commented in the view of Fig. 14. This fact highlights that any ligament length comparisons with experimental data are not fully representative unless flapping is also taken into account.
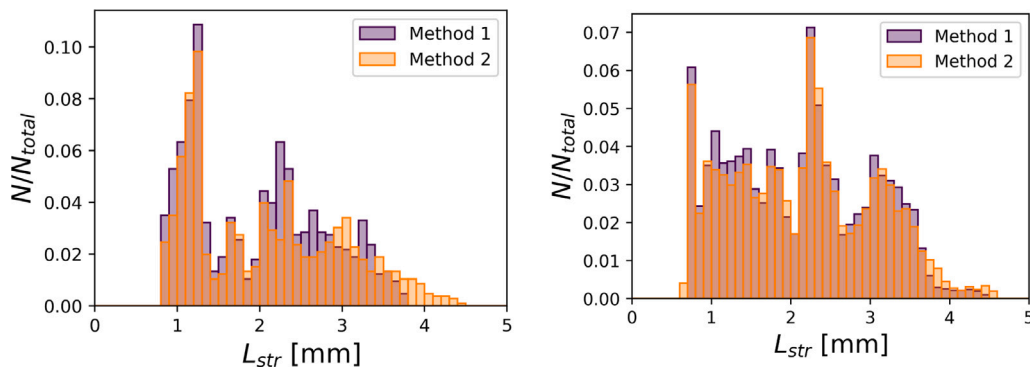
Fig. 16. Comparison among the ligament 2D length distributions found for Method 1 and Method 2 for the $h_l \neq f(t,z)$ case (left) and $h_l = f(t,z)$ case (right).
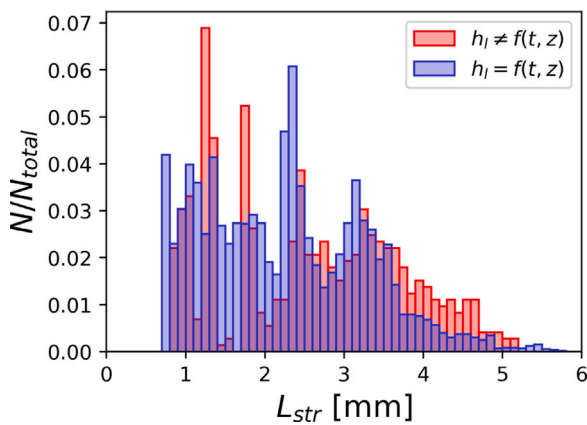

Fig. 17. Ligament 3D length distributions found for both simulated test cases (Method 2 used for ligament length measurement).

As far as ligament tip velocities $\mathbf{u_{str}}$ are concerned, the distributions obtained for each of the three components in each simulated case are shown in Fig. 18. Important differences are found in all cases. Focusing on the streamwise velocity component, the distribution for the $h_l \neq f(t,z)$ case is significantly shifted towards higher values (the distribution is centered around $u/u_g = 0.12$) than the distribution for the $h_l = f(t,z)$ case (most ligaments found in the $u/u_g = 0$ to 0.1 range). This may be explained considering the locations at which it is more probable to find a ligament tip in each simulated case, shown in Fig. 19. In the $h_l \neq f(t,z)$ case, the liquid film flaps more importantly about the prefilmer center line (recall also Fig. 14). Thus, in this case the ligaments extend towards more external wall-normal locations, where the influence from the liquid and gas–liquid boundary layers is less severe. At these locations the gaseous phase travels faster, leading to a greater momentum exchange with the liquid film and the resulting ligaments, increasing their axial velocities. The locations at which the ligament tips are found also explain the different distributions obtained in Fig. 18 for the wall-normal ligament tip velocity components: the $h_l = f(t,z)$ case resembles a normal distribution centered about $v/u_g = 0$, as the ligament tips are equally found around the prefilmer center line in Fig. 19. However, the $h_l \neq f(t,z)$ case yields a bimodal distribution, one of the modes being centered around a value $v/u_g \geq 0$. This mode corresponds to the fact that, in this case, the ligament tips are preferentially found above the prefilmer edge (see Fig. 19) or close to its center (please note that this result might be biased by the fact that only 3 breakup events could be simulated, potentially not resulting in a statistically representative sample in this strategy). Ligaments that extend above the prefilmer tend to move away from the prefilmer surface in the wall-normal direction as they penetrate axially,

thus possessing positive wall-normal velocities. Finally, the differences among test cases in the spanwise component distributions are less severe, being centered around $w/u_g = 0$ in both cases. The deviation about this value is more acute in the $h_l \neq f(t,z)$ case, since the film disintegration into ligaments is more violent in this simulation.

Fig. 20 depicts the histogram of ligament equivalent diameters d_{eq} for both simulated cases. For each distribution, there are several peaks or clusters of ligaments with similar equivalent diameter. Hence, it may be expected that the sizes of the droplets generated from ligament breakup are related to these values. However, since the ligament equivalent diameter embeds the evolution of the ligament diameter along its length, the quantitative values cannot be directly comparable to drop size diameter values (droplets generated by ligament breakup are strictly generated at the ligament tip). Anyway, the qualitative comparison among simulation methodologies is insightful, as a strong influence of the simulated test case is observed on the processed data. In the $h_l \neq f(t,z)$ case, equivalent diameters are shifted towards significantly lower values than their $h_l = f(t,z)$ counterpart. It may then be expected for the droplets generated from ligament breakup in the $h_l \neq f(t,z)$ case to have statistically lower sizes than the droplets generated from ligament breakup in the $h_l = f(t,z)$ case. A closer look at this phenomenon will be given in the analysis of the droplet cloud generated in each simulation.

Finally, characteristic quantities from the ligament analysis are displayed in Table 6. As expected according to the view of the size PDFs, the mean breakup length L_{bu} is sensibly underpredicted in all cases, but it reaches values similar to the literature DNS (Warncke et al., 2017; Mukundan et al., 2022). The 2D analysis used for validation shows that the breakup length prediction for the $h_l = f(t,z)$ case is slightly closer to the literature data. This fact, together with a better prediction of u_{def}, leads to a better agreement in mean breakup frequency f_{bu} than the one obtained through the $h_l \neq f(t,z)$ case, although the value is overpredicted compared to the experiments due to the large underprediction in breakup length. In any case, it is observed that mean values may not be representative of the agreement in the related distributions. The values extracted through the developed 3D analysis show that the breakup length is more noticeably increased from the 2D values in the $h_l \neq f(t,z)$ case than in the $h_l = f(t,z)$ case, due to the larger extension of the ligaments in the wall-normal direction found for this case. The film deformation velocity is however reduced, thus leading to lower breakup frequencies if they are computed from the 3D analysis.

4.2.2. Droplet cloud results

The post-processing technique described in Section 3.3.4 allowed detecting distinct droplets in both simulated cases. The temporal evolution of the number of detected droplets in each simulation is shown in Fig. 21, where the initial transient has been omitted and results are normalized with the mean amount of droplets detected in the depicted interval. These values are 406 droplets/frame in the $h_l \neq f(t,z)$ case
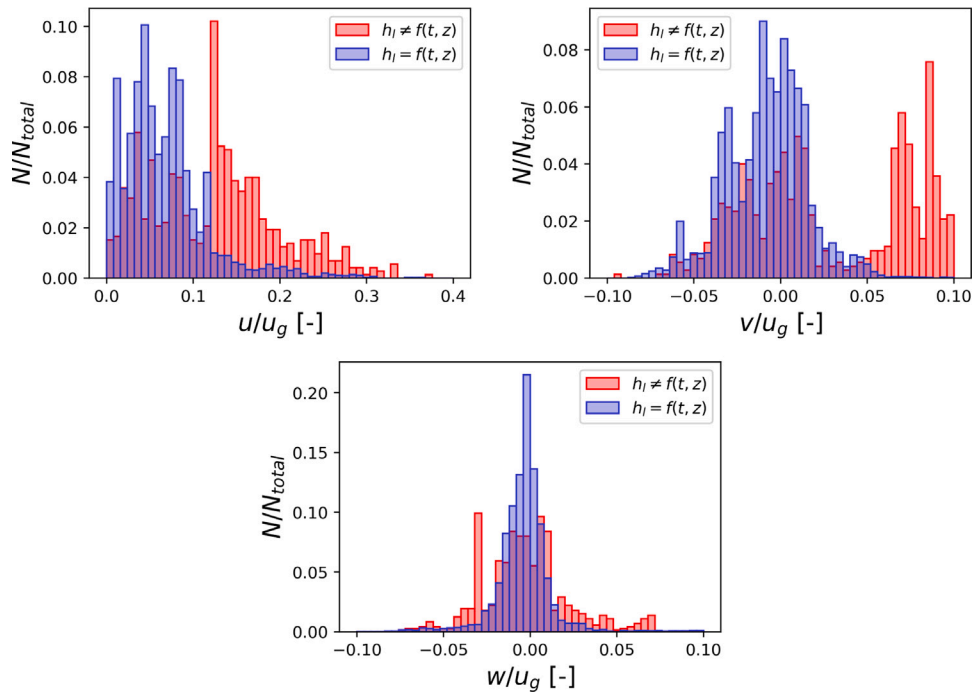
Fig. 18. Distributions of 3D ligament tip velocity components for both simulated test cases: streamwise velocity (top left), wall-normal velocity (top right), spanwise velocity (bottom). All values are normalized with the gas bulk velocity.
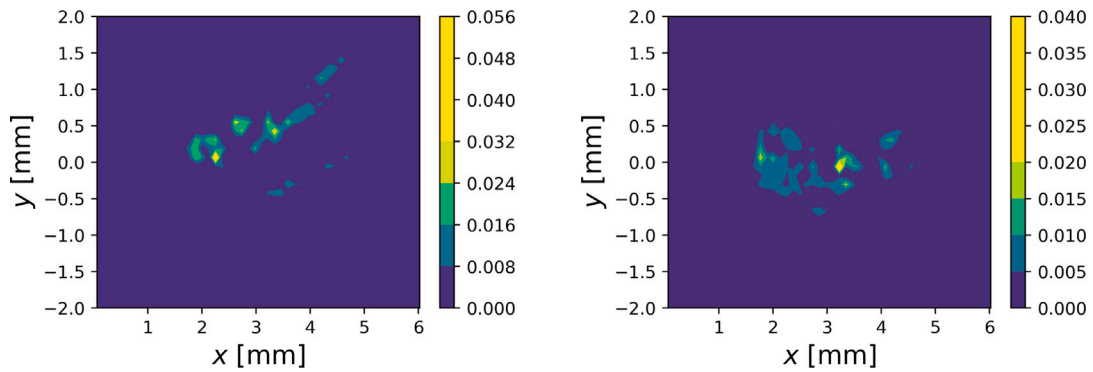

Fig. 19. Contours displaying the probability of finding a ligament tip in the different locations of the XY plane: $h_l \neq f(t, z)$ case (left) and $h_l = f(t, z)$ case (right).
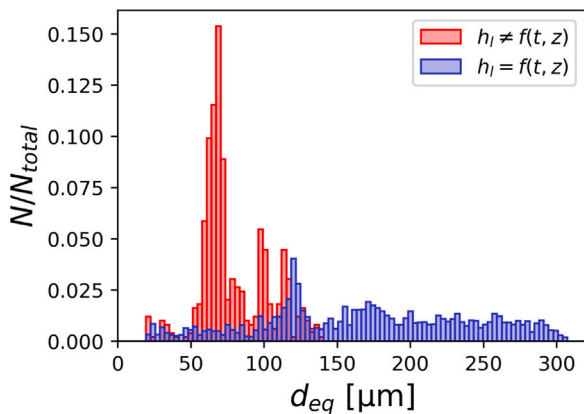

Fig. 20. Ligament equivalent diameter distributions found for both simulated test cases (Method 2 used for ligament length measurement, only 3D data considered).

Table 6

Characteristic quantities obtained from the ligament 2D and 3D analysis for both simulations and size post-processing methods. Literature DNS and literature experimental data from Warncke et al. (2017) are also provided. Note: the u_{lig} value of the literature experimental data was found for $\dot{V}/b = 25$ mm²/s.

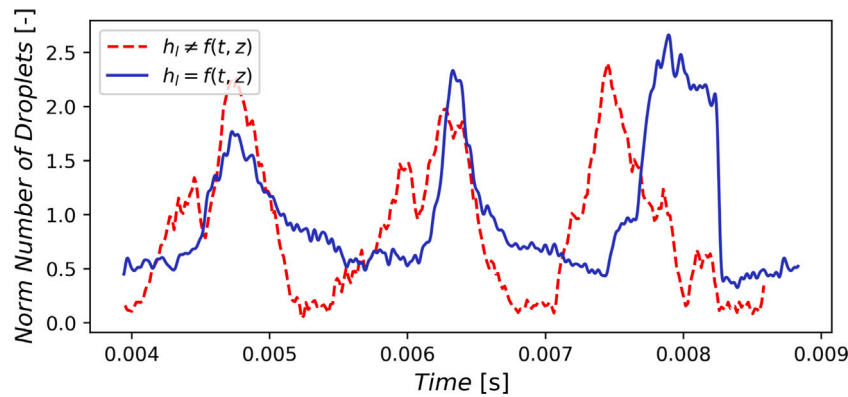| Source	L_{bu} [mm]	u_{lig} [m/s]	u_{def} [m/s]	f_{bu} [kHz]
Lit. Exp. 2D (Gepperth et al., 2012)	3.2	5.00	–	4.91
Lit. DNS 2D (Warncke et al., 2017)	2.2	–	8.2	3.73
$h_l \neq f(t, z)$ 2D	2.0	5.79	6.53	3.27
$h_l = f(t, z)$ 2D	2.1	6.2	11.97	5.70
$h_l \neq f(t, z)$ 3D	2.56	6.87	6.28	2.45
$h_l = f(t, z)$ 3D	2.25	3.50	11.51	5.12

Fig. 21. Temporal evolution of the number of detected droplets for both simulated cases. Results are normalized with the mean number of droplets detected in the time series in each case: 406 droplets for the $h_l \neq f(t,z)$, 62 droplets for the $h_l = f(t,z)$ case.

and 62 droplets/frame in the $h_l = f(t,z)$ case. These large variation could be appreciated from the flow evolution depicted in Fig. 14. While other literature works using VOF on the test case did not specifically report this quantity, their qualitative comparisons among experimental and computational snapshots also showed a clear overprediction of the amount of droplets computationally simulated (especially noticeable in the side views, considering the actual prefilmer span b is an order of magnitude greater than the simulated span) (Warncke et al., 2017; Mukundan et al., 2022). This fact is aligned with the finding of the present investigation, in the sense that accounting for the liquid film evolution upstream of the prefilmer edge results in a less violent breakup and a substantially lower amount of generated droplets.

Coming back to Fig. 21, it is possible to distinguish three main breakup events where the number of droplets suddenly increases, substantially rising above the average. These instants correspond to the stages of *bag breakup* illustrated in Fig. 14. After a main breakup event, the number of generated droplets decreases as only ligament breakup is present while liquid is being accumulated in the reservoir behind the prefilmer edge prior to a new bag breakup event. Important differences are observed among the simulated cases. In the $h_l \neq f(t,z)$ case, the amount of generated droplets after a main event decays practically down to zero, importantly inhibiting atomization. In the $h_l = f(t,z)$ case, however, the amount of generated droplets only gets down to half of the average amount. This implies that ligament breakup is more relevant in this case and atomization is more continuous. As discussed in the view of Fig. 21, the fact that temporal and spanwise variations in the film thickness are included at the DNS inlet results in film waves reaching the liquid reservoir behind the perfilmer edge in a non-synchronized manner. Hence, the film reservoir is not uniform spanwise and bags are not generated along the whole span by the time some of them break. This yields a less violent main bag breakup event and a greater relative importance of the ligament breakup, as the resulting ligaments are also shaped by the remaining reservoir prior to the formation of new bags.

Additionally, the frequency among main events also differs for both simulations. A value of $f_{main} = 656.2$ Hz is observed for the $h_l \neq f(t,z)$ case, whereas $f_{main} = 630.0$ Hz is found for the $h_l = f(t,z)$ case. Even though both values are similar to the reported $\overline{f_{film}} = 585.9$ Hz from the 2-phase flow precursor LES (recall Table 5), the $h_l = f(t,z)$ case is closer, despite not accounting for the effect of the interfacial instability on the complete prefilming surface. Holz et al. (2018) already reported a direct relation among film wave frequency and breakup frequency, but justifying the minor differences through the slight decoupling by the accumulation of liquid at the trailing edge. This also justifies the differences observed in the present study among film wave frequency and breakup frequency. Even though the decoupling is present, not the same breakup frequency is retrieved if the film wave behavior is not introduced to the DNS. While this decoupling

among frequencies is observed for this operating condition with $M = 15.7$, it must be noted that operating conditions with higher momentum flux ratios (Fernandez et al., 2009) or with a lower ratio among film thickness and prefilmer thickness (Inamura et al., 2019) (as is the case of commonly used aero engines) are expected to become dominated by the film evolution rather than by liquid accumulation. In such cases, the presented results highlight the importance of accounting for the liquid film evolution upstream of the prefilmer edge, either through the inlet boundary condition proposed in the study (one-way coupling among domains), or by means of a larger computational domain for two-way coupling hardly affordable currently.

As far as the droplet sizes are concerned, Fig. 22 shows the drop diameter PDFs for both simulated cases compared against experimental data. As mentioned in Section 3.3.4, it is important to note that droplets exhibiting a diameter $d_v \leq 20\,\mu$m have been discarded from the analysis, also corresponding to the resolution limit of the experimental data (Warncke et al., 2017). The comparison highlights that a substantially fairer agreement with experimental data is achieved when accounting for the liquid film history in the $h_l = f(t,z)$ case. This result may be justified in the view of the ligament equivalent diameter (d_{eq}) distributions (Fig. 20): droplets generated from ligament breakup in the $h_l \neq f(t,z)$ case have statistically lower sizes (comparable to the ones generated from bag breakup) than the droplets generated from ligament breakup in the $h_l = f(t,z)$ case (which are significantly larger than the ones generated from bag breakup). This explains why the drop size PDF of the $h_l \neq f(t,z)$ case seems to have a single mode, as the ligament breakup mechanism is obscured by the large amount of droplets produced at the bag burst stage. The drop size PDF of the $h_l = f(t,z)$ case, in turn, recovers a multi-modal distribution, since the droplets generated from ligament breakup are substantially larger than the ones generated from bag breakup. The fact that the multi-modal distribution is recovered when accounting for the liquid film thickness evolution upstream of the prefilmer edge implies that this simulation correctly balanced the relative importance among *bag breakup* and *ligament breakup*, better resembling the experimental results despite showing a slight underprediction of the size values of the peaks in the first two modes.

Fig. 23 shows the PDFs obtained for each of the droplet velocity components, including a comparison with experimental data from Warncke et al. (2017) in the case of the streamwise component. Despite the differences in the number of predicted droplets and their size PDFs, the distributions are relatively similar among simulated cases. In the case of the streamwise velocity component, both predicted PDFs resemble a normal distribution. The agreement with experimental data seems slightly better in the $h_l = f(t,z)$ case, although values are underpredicted for a relevant amount of droplets. The distribution shape and dispersion about the average is similar for both simulated cases, but the distribution is shifted towards larger velocities in the $h_l \neq f(t,z)$ case.
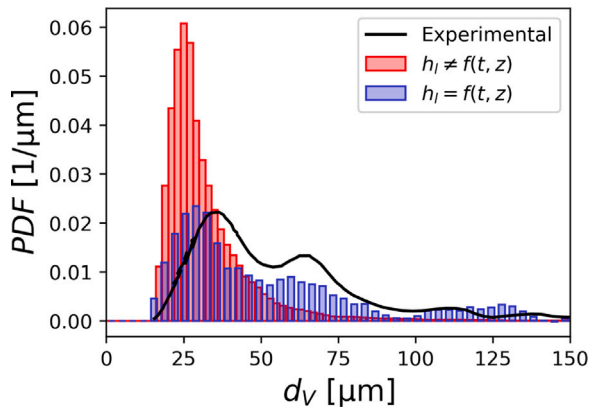
Fig. 22. Droplet size Probability Density Function (PDF) for both simulations and experimental data from Warncke et al. (2017).

This fact is reasonable considering that a larger proportion of small droplets (subject to less aerodynamic drag when interacting with the gaseous phase) was found, and results in a substantial overprediction compared to experimental data. As far as the wall-normal velocities are concerned, the PDF is centered around 0 for the $h_l = f(t, z)$ case, exhibiting low dispersion. Nevertheless, the $h_l \neq f(t, z)$ case predicts a noticeably higher dispersion and its average is displaced towards negative values. As it happened for the ligament tips, this may be explained considering the locations at which it is more probable to find a droplet in each simulated case, as shown in Fig. 24. As already explained in the view of Fig. 14, in the $h_l \neq f(t, z)$ case the liquid film flaps more importantly about the prefilmer center line, resulting in a wider spray angle. Fig. 24 also highlights that droplets in the $h_l \neq f(t, z)$ case are preferentially found below the prefilmer center line, whereas they are quite uniformly distributed on both sides of the prefilmer in the $h_l = f(t, z)$ case. It is important to recall that, in the former case, ligaments were preferentially found above the prefilmer, as shown in Section 4.2.1. Fig. 14 showed a situation for this case for which ligaments indeed extended above the prefilmer. Such ligaments were generated from a film flapping motion whose bags got punctured towards the opposite side of the prefilmer, yielding a substantially higher amount of droplets below the prefilmer center line. Droplets generated below the prefilmer through this mechanism tend to travel further away from the prefilmer center line, reaching negative wall-normal velocities as reflected in Fig. 23. In any case, it must be again noted that this shift towards negative wall-normal velocities may be biased by the fact that only 3 breakup events could be simulated. Results for the $h_l = f(t, z)$ case seem more statistically representative as the film accumulation behind the prefilmer edge is desynchronized spanwise, providing bag breakup both above and below the prefilmer center line and resulting in a spray more uniformly spread in the wall-normal direction. Finally, the differences among simulated cases in the spanwise component distributions are not so relevant, being centered around $w/u_g = 0$ in both cases and slightly more deviated about this value in the $h_l \neq f(t, z)$ case.

It is interesting to analyze the correlation among droplet size and droplet velocity. Fig. 25 (left) shows the scattered information (focused on streamwise velocity) for all the detected droplets in both simulated cases. Results show that in both simulated cases large droplets statistically possess a lower streamwise velocity. Additionally, the dispersion in the velocity PDF is greater the lower the drop size, as confirmed in the view of Fig. 25 (right) where it is seen that the mean velocities are noticeably shifter towards high values as the droplet size decreases. These trends follow a non-linear fashion. As already implied by Fig. 23, the comparison among test cases highlights the greater velocities achieved by the droplet cloud in the $h_l \neq f(t, z)$ case compared to the $h_l = f(t, z)$ case.

5. Summary and conclusions

In the present work, a numerical investigation on planar prefilming airblast primary breakup was conducted through a VOF-DNS method. A novel approach was presented to account for the spatio-temporal evolution of the liquid film thickness upstream of the prefilmer edge. Assuming the flow between computational domains as one-way coupled, this methodology required the computation of subsequent single-phase and two-phase flow LES to gather data to include at the DNS inflow boundary condition, considering the DNS domain had to be restricted to the last part of the prefilmer and the first millimetres downstream of its edge. These precursor simulations were successfully validated against consolidated channel flow DNS data and experimental data, respectively. Additionally, a methodology to post-process ligament data not only in a 2D projection but in a 3D domain was also proposed.

Results for an operating condition widely studied in the literature were discussed comparing two DNS simulations with different inflow conditions: a DNS that only accounted for a constant (timewise and spanwise) liquid film thickness at the domain inlet on the one hand; and the DNS that took advantage of the full proposed methodology by accounting for the oscillations in the liquid film thickness at the domain inlet on the other hand. The inflow condition of both simulations accounted for gas turbulence.

Qualitative comparisons among the primary breakup simulations showed important differences among simulation strategies. Even though the predicted breakup mechanism sequence was the same in accordance with the momentum flux ratio of the chosen operating condition (liquid accumulation behind the prefilmer edge followed by bag formation, bag breakup, ligament formation and ligament breakup), the resulting ligament distribution and droplet cloud were fairly different. Accounting for the liquid film evolution upstream of the prefilmer edge resulted in the liquid reservoir formed behind its edge being less uniformly distributed spanwise than it was for the constant liquid film thickness case, as the film crests and valleys do not reach the reservoir in a synchronized manner along the prefilmer span. This eventually results in a less violent main bag breakup event when the film evolution upstream of the prefilmer edge is accounted for, inhibiting atomization to a certain extent but producing breakup more continuously in time than for the constant liquid film thickness case. Even though both simulation strategies lead to a substantially greater amount of droplets being generated by bag breakup than by ligament breakup, the latter mechanism gains relative importance when accounting for the liquid film evolution upstream of the prefilmer edge. Additionally, ligaments predicted through this methodology have a statistically larger equivalent diameter than the ones predicted when the film evolution is not considered. This allowed the prediction of a clearly multimodal drop size distribution in this case.

DNS ligament and droplet cloud processed data were quantitatively validated against experimental results available in the literature. A reasonable agreement was found in both simulated cases, with a noticeable improvement in the predictions when accounting for the liquid film evolution upstream of the prefilmer edge, despite not accounting for the absolute nature of the interfacial instability produced at this location. The multi-modal feature of the droplet size distribution exhibited by the experiments could only be retrieved when making use of the proposed methodology, as explained above. The observed differences in the velocity distributions, splitted among velocity components, could be explained by the fact that the spray was differently spread in the wall-normal direction in both cases. Accounting for the liquid film evolution along the prefilmer surface resulted in a uniformly spread spray within a relatively narrow cone. However, the constant liquid film thickness case resulted in a wider spray due to the greater importance achieved by film flapping in this case. In this simulation, the film behaves similarly at all spanwise locations for a given breakup event, meaning that all the shaped bags get punctured and break up at the same stage of flapping, generating all droplets at the same side of the prefilmer,
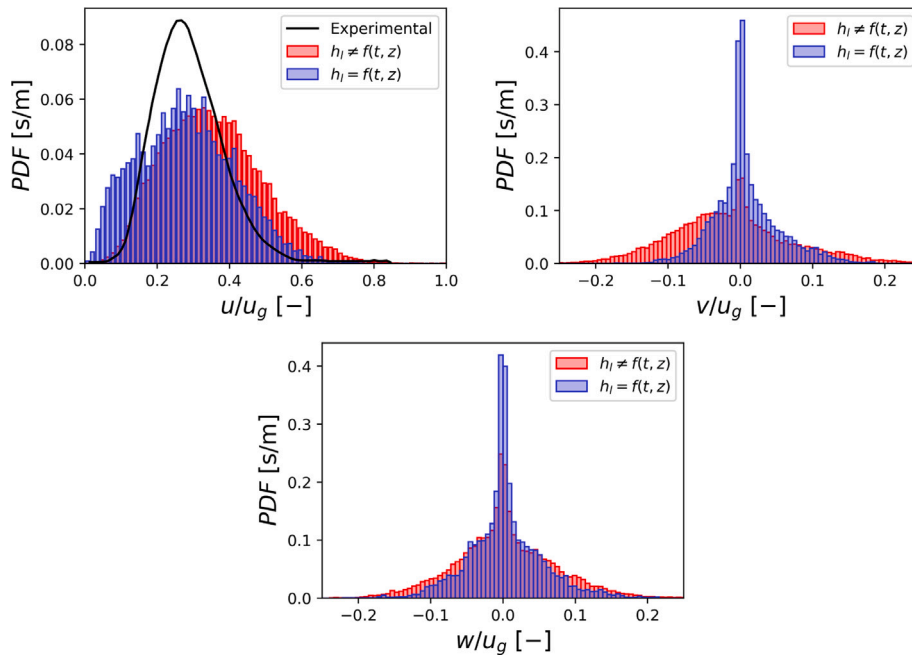
Fig. 23. PDFs for the droplet velocity components for both simulated test cases: streamwise velocity (top left, including also experimental data from Warncke et al. (2017)), wall-normal velocity (top right), spanwise velocity (bottom). All values are normalized with the gas bulk velocity.
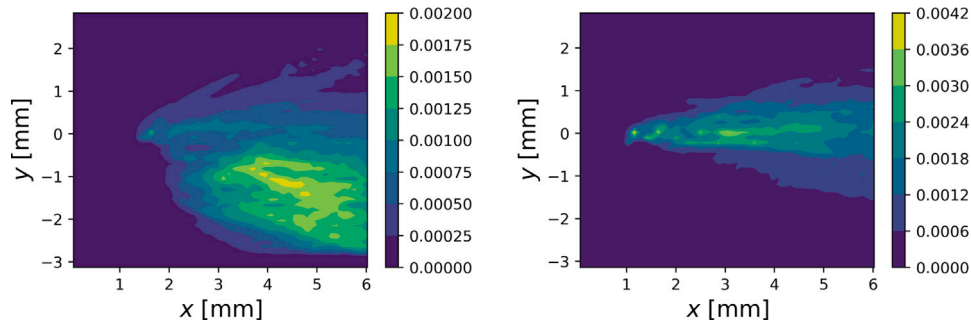

Fig. 24. Contours displaying the probability of finding a droplet in the different locations of the XY plane: $h_l \neq f(t, z)$ case (left) and $h_l = f(t, z)$ case (right).
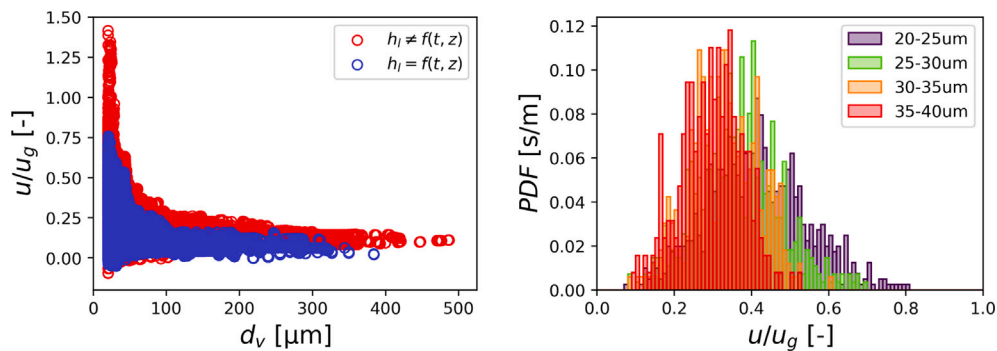

Fig. 25. Scatter plot for the streamwise droplet velocity as a function of the drop diameter for both simulated cases (left), and detail on the streamwise droplet velocity PDFs corresponding to different drop size classes in the $h_l \neq f(t, z)$ case (right).

thereby also conditioning their velocities. In any case, the averaged and aggregated quantities considered in the analysis of the constant liquid film thickness case might be biased by the fact that only a few distinct breakup events were simulated and not accounting for a wide range of variability of breakup events. This limitation is in fact attenuated if the liquid film evolution along the prefilmer surface is accounted for.

Additionally to the commented shortcoming concerning the realizable simulated time, other limitations of the methodology must be highlighted. The large amount of resources required for the calculations implied only a small computational domain could be considered. This fact hindered the characterization of the ligament formation stage, as the experiments reported longer ligaments than the ones possibly found

in the simulations. Nevertheless, this limitation is acknowledged in most literature works achieving a similar resolution than the one here presented. Precisely the mesh resolution is another limitation. Even though a proper turbulence reproduction was ensured by comparison with the Kolmogorov length scale, achieving lower cell sizes would have resulted in a better description of the liquid–gas interface, as a large amount of droplets was found to have diameters in the order of twice the cell size. Moreover, the artificial instability triggered by the prefilmer edge is of absolute nature, implying said instability is also transmitted upstream of the generating source. This phenomenon is not fully accounted for in the proposed methodology, which splits the geometry in different computational domains assuming one-way coupling among them. The upstream effect of this instability is thus only accounted for in the limited part of the DNS domain covering the prefilming surface.

Finally, it must be noted that the study is restricted to a given operating condition corresponding to the torn sheet breakup regime, for which liquid accumulation behind the prefilmer edge is significant and the breakup frequency is partially decoupled from the film wave frequency. Conditions with a higher gas-to-liquid momentum flux ratio, realizable in aero engines, lead to the so-called membrane sheet breakup, where the accumulation mechanism loses importance in favor of a direct disintegration in ligaments and droplets behind the prefilmer edge. In such circumstances the breakup frequency is expected to be more closely coupled to the film wave frequency. This should result in a more realistic description and more accurate predictions being obtained by the methodology proposed in the present investigation.

CRediT authorship contribution statement

R. Payri: Conceptualization, Resources, Supervision, Project administration, Funding acquisition. **F.J. Salvador:** Conceptualization, Methodology, Formal analysis, Writing – review & editing. **M. Carreres:** Conceptualization, Methodology, Validation, Investigation, Writing – original draft, Writing – review & editing. **C. Moreno-Montagud:** Methodology, Software, Investigation, Writing – original draft, Writing – review & editing, Visualization.

Declaration of competing interest

The authors declare that they have no known competing financial interests or personal relationships that could have appeared to influence the work reported in this paper.

Data availability

Data will be made available on request.

Acknowledgments

References

Agbaglah, G., Chiodi, R., Desjardins, O., 2017. Numerical simulation of the initial destabilization of an air-blasted liquid layer. J. Fluid Mech. 812, 1024–1038. http://dx.doi.org/10.1017/jfm.2016.835.

Aniszewski, W., Arrufat, T., Crialesi-Esposito, M., Dabiri, S., Fuster, D., Ling, Y., Lu, J., Malan, L., Pal, S., Scardovelli, R., Tryggvason, G., Yecko, P., Zaleski, S., 2021. Parallel, robust, interface simulator (PARIS). Comput. Phys. Comm. 263, http://dx.doi.org/10.1016/j.cpc.2021.107849, arXiv:2012.11744.

Aniszewski, W., Bogusławski, A., Marek, M., Tyliszczak, A., 2012. A new approach to sub-grid surface tension for LES of two-phase flows. J. Comput. Phys. 231 (21), 7368–7397. http://dx.doi.org/10.1016/j.jcp.2012.07.016.

Berthoumieu, P., Lavergne, G., 2001. Video techniques applied to the characterization of liquid sheet breakup. J. Vis. 4 (3), 267–275. http://dx.doi.org/10.1007/BF03182587.

Brackbill, J.U., Kothe, D.B., Zemach, C., 1992. A continuum method for modeling surface tension. J. Comput. Phys. 100 (2), 335–354. http://dx.doi.org/10.1016/0021-9991(92)90240-Y, URL https://linkinghub.elsevier.com/retrieve/pii/002199919290240Y.

Bradski, G., 2000. The OpenCV library. Dr. Dobb's J. Software Tools 25 (11), 120–125.

Braun, S., Wieth, L., Holz, S., Dauch, T.F., Keller, M.C., Chaussonnet, G., Gepperth, S., Koch, R., Bauer, H.J., 2019. Numerical prediction of air-assisted primary atomization using smoothed particle hydrodynamics. Int. J. Multiph. Flow. 114, 303–315. http://dx.doi.org/10.1016/j.ijmultiphaseflow.2019.03.008.

Carmona, J., Odier, N., Desjardins, O., Cuenot, B., Misdariis, A., Cayre, A., 2021. A comparative study of direct numerical simulation and experimental results on a prefilming airblast atomization configuration. At. Spray. 31 (8), 9–32. http://dx.doi.org/10.1615/ATOMIZSPR.2021037399.

Chaussonnet, G., Gepperth, S., Holz, S., Koch, R., Bauer, H.J., 2020. Influence of the ambient pressure on the liquid accumulation and on the primary spray in prefilming airblast atomization. Int. J. Multiph. Flow. 125, 103229. http://dx.doi.org/10.1016/j.ijmultiphaseflow.2020.103229, arXiv:1906.04042.

Chaussonnet, G., Laroche, T., Lieber, C., Holz, S., Koch, R., Bauer, H.-J., 2018. Investigation of the liquid accumulation characteristics in planar prefilming airblast atomization. In: ICLASS 2018 - 14th International Conference on Liquid Atomization and Spray Systems. Chicago, IL.

Chaussonnet, G., Müller, A., Holz, S., Koch, R., Bauer, H.J., 2017. Time-response of recent prefilming airblast atomization models in an oscillating air flow field. J. Eng. Gas Turbines Power 139 (12), http://dx.doi.org/10.1115/1.4037325.

Chaussonnet, G., Vermorel, O., Riber, E., Cuenot, B., 2016. A new phenomenological model to predict drop size distribution in Large-Eddy Simulations of airblast atomizers. Int. J. Multiph. Flow. 80, 29–42. http://dx.doi.org/10.1016/j.ijmultiphaseflow.2015.10.014.

Crank, J., Nicolson, P., 1947. A practical method for numerical evaluation of solutions of partial differential equations of the heat-conduction type. Math. Proc. Camb. Phil. Soc. 43 (1), 50–67. http://dx.doi.org/10.1017/S0305004100023197.

Crialesi-Esposito, M., Gonzalez-Montero, L.A., Salvador, F.J., 2022. Effects of isotropic and anisotropic turbulent structures over spray atomization in the near field. Int. J. Multiph. Flow. 150, http://dx.doi.org/10.1016/j.ijmultiphaseflow.2021.103891.

Deshpande, S.S., Anumolu, L., Trujillo, M.F., 2012. Evaluating the performance of the two-phase flow solver interFoam. Comput. Sci. Discov. 5, 014016. http://dx.doi.org/10.1088/1749-4699/5/1/014016.

Fernandez, V.G., Berthoumie, P., Lavergne, G., 2009. Liquid sheet disintegration at high pressure: An experimental approach. C. R. - Mec. 337 (6–7), 481–491. http://dx.doi.org/10.1016/j.crme.2009.06.026.

Fuster, D., Matas, J.-P., Marty, S., Popinet, S., Hoepffner, J., Cartellier, A., Zaleski, S., 2013. Instability regimes in the primary breakup region of planar coflowing sheets. J. Fluid Mech. 736, 150–176. http://dx.doi.org/10.1017/jfm.2013.536.

Gepperth, S., Bärow, E., Koch, R., Bauer, H., 2014. Primary atomization of prefilming airblast nozzles : Experimental studies using advanced image processing techniques. In: 26th Annual Conference on Liquid Atomization and Spray Systems. pp. 1–15.

Gepperth, S., Guildenbecher, D., Koch, R., Bauer, H.-J., 2010. Pre-filming primary atomization: Experiments and modeling. In: ILASS - Europe 2010, 23rd Annual Conference on Liquid Atomization and Spray Systems. Brno (Czech Republic).

Gepperth, S., Müller, A., Koch, R., Bauer, H.-J., 2012. Ligament and droplet characteristics in prefilming airblast atomization. In: ICLASS 2012, 12th Triennial International Conference on Liquid Atomization and Spray Systems. Heidelberg (Germany).

Greenshields, C., Weller, H., 2022. Notes on Computational Fluid Dynamics: General Principles. CFD Direct Ltd, Reading, UK.

Herrmann, M., 2013. A sub-grid surface dynamics model for sub-filter surface tension induced interface dynamics. Comput. & Fluids 87, 92–101. http://dx.doi.org/10.1016/j.compfluid.2013.02.008.

Holz, S., Braun, S., Chaussonnet, G., Dauch, T.F., Kaden, J., Keller, M., Schwitzke, C., Koch, R., Bauer, H.-J., 2018. New insights in the primary breakup process of prefilming airblast atomizers by SPH predictions. In: ICLASS 2018, 14th Triennial International Conference on Liquid Atomization and Spray Systems. Chicago, IL.

Holz, S., Chaussonnet, G., Gepperth, S., Koch, R., Bauer, H.-J., 2016. Comparison of the primary atomization model PAMELA with drop size distributions of an industrial prefilming airblast nozzle. In: ILASS - Europe 2016, 27th Annual Conference on Liquid Atomization and Spray Systems.

Inamura, T., Katagata, N., Nishikawa, H., Okabe, T., Fumoto, K., 2019. Effects of prefilmer edge thickness on spray characteristics in prefilming airblast atomization. Int. J. Multiph. Flow. 121, 103117. http://dx.doi.org/10.1016/j.ijmultiphaseflow.2019.103117.

Inamura, T., Shirota, M., Tsushima, M., Kato, M., Hamajima, S., Sato, A., 2012. Spray characteristics of prefilming type of airblast atomizer. In: ICLASS 2012 - 12th International Conference on Liquid Atomization and Spray Systems.

Issa, R., 1986. Solution of the implicitly discretised fluid flow equations by operator-splitting. J. Comput. Phys. 62 (1), 40–65. http://dx.doi.org/10.1016/0021-9991(86)90099-9.

Iwamoto, K., Suzuki, Y., Kasagi, N., 2002. Reynolds number effect on wall turbulence: Toward effective feedback control. Int. J. Heat Fluid Flow 23 (5), http://dx.doi.org/10.1016/S0142-727X(02)00164-9.

Jasuja, A.K., 2006. Behaviour of aero-engine airblast sprays in practical environments. In: 10th International Conference on Liquid Atomization and Spray Systems. ICLASS 2006, Kyoto, Japan.

Jiang, D., Ling, Y., 2020. Destabilization of a planar liquid stream by a co-flowing turbulent gas stream. Int. J. Multiph. Flow. 122, 103121. http://dx.doi.org/10.1016/j.ijmultiphaseflow.2019.103121.

Jiang, D., Ling, Y., 2021. Impact of inlet gas turbulence on the formation, development and breakup of interfacial waves in a two-phase mixing layer. J. Fluid Mech. 921, A15. http://dx.doi.org/10.1017/jfm.2021.481.

Jofre, L., Dodd, M.S., Grau, J., Torres, R., 2020. Near-interface flow modeling in large-eddy simulation of two-phase turbulence. Int. J. Multiph. Flow. 132, http://dx.doi.org/10.1016/j.ijmultiphaseflow.2020.103406.

Kajishima, T., Taira, K., 2017. Computational Fluid Dynamics, first ed. Springer International Publishing, Cham, Switzerland, http://dx.doi.org/10.1007/978-3-319-45304-0.

Kim, Y.J., Bouscasse, B., Seng, S., Le Touze, D., 2019. Numerical study on the temporal discretization schemes in two-phase wave simulation. In: International Conference on Offshore Mechanics and Arctic Engineering (OMAE 19), Volume 2: CFD and FSI. American Society of Mechanical Engineers, http://dx.doi.org/10.1115/OMAE2019-96278.

Koch, R., Braun, S., Wieth, L., Chaussonnet, G., Dauch, T., Bauer, H.-J., 2017. Prediction of primary atomization using smoothed particle hydrodynamics. Eur. J. Mech. B/Fluids 61, 271–278. http://dx.doi.org/10.1016/j.euromechflu.2016.10.007.

Lacis, U., Pellegrino, M., Sundin, J., Amberg, G., Zaleski, S., Hess, B., Bagheri, S., 2022. Nanoscale sheared droplet: Volume-of-fluid, phase-field and no-slip molecular dynamics. J. Fluid Mech. 940, 1–45. http://dx.doi.org/10.1017/jfm.2022.219.

Lee, S.B., 2017. A study on temporal accuracy of OpenFOAM. Int. J. Naval Architect. Ocean Eng. 9 (4), 429–438. http://dx.doi.org/10.1016/j.ijnaoe.2017.03.007.

Lefebvre, A.H., McDonell, V.G., 2017. Atomization and Sprays, second ed. CRC Press.

Legendre, D., Maglio, M., 2015. Comparison between numerical models for the simulation of moving contact lines. Comput. & Fluids 113, 2–13. http://dx.doi.org/10.1016/j.compfluid.2014.09.018.

Li, J., 1995. Calcul d'interface affine par morceaux (piecewise linear interface calculation). C. R. Acad. Sci. Paris, II 320, 391–396.

Liu, Y., Sun, X., Sethi, V., Nalianda, D., Li, Y.G., Wang, L., 2017. Review of modern low emissions combustion technologies for aero gas turbine engines. Prog. Aerosp. Sci. 94 (July), 12–45. http://dx.doi.org/10.1016/j.paerosci.2017.08.001.

Matas, J.P., Marty, S., Dem, M.S., Cartellier, A., 2015. Influence of gas turbulence on the instability of an air-water mixing layer. Phys. Rev. Lett. 115 (7), http://dx.doi.org/10.1103/PhysRevLett.115.074501.

Matsuura, K., Suzuki, K., Kurosawa, Y., 2008. Effects of ambient pressure on spray characteristics of a high-shear-type aero-engine airblast fuel injector. In: ILASS 2008. Como Lake, Italy.

Mosbach, T., Sadanandan, R., Meier, W., Eggels, R., 2010. Experimental analysis of altitude relight under realistic conditions using laser and high-speed video techniques. In: Volume 2: Combustion, Fuels and Emissions, Parts a and B. ASMEDC, pp. 523–532. http://dx.doi.org/10.1115/GT2010-22625.

Moser, R.D., Kim, J., Mansour, N.N., 1999. Direct numerical simulation of turbulent channel flow up to Reτ=590. Phys. Fluids 11 (4), 943–945. http://dx.doi.org/10.1063/1.869966.

Mukundan, A.A., Ménard, T., Berlemont, A., César, J., Mukundan, A.A., Ménard, T., Berlemont, A., César, J., Motta, B.D., 2019a. Validation and analysis of 3D DNS of planar pre-filming airblast atomization simulations to cite this version. In: ILASS Americas, 30th Annual Conference on Liquid Atomization and Spray Systems. Tempe, Arizona.

Mukundan, A.A., Ménard, T., Berlemont, A., de Motta, J.C.B., 2019b. A comparative study of DNS of airblast atomization using CLSMOF and CLSVOF methods. In: ILASS - Europe 2019, 29th Conference on Liquid Atomization and Spray Systems.

Mukundan, A.A., Ménard, T., de Motta, J.C.B., Berlemont, A., 2022. Detailed numerical simulations of primary atomization of airblasted liquid sheet. Int. J. Multiph. Flow. 147, http://dx.doi.org/10.1016/j.ijmultiphaseflow.2021.103848.

Nicoud, F., Ducros, F., 1999. Subgrid-scale stress modelling based on the square of the velocity gradient tensor. Flow Turbul. Combust. 62 (3), 183–200. http://dx.doi.org/10.1023/A:1009995426001, arXiv:arXiv:1503.01439v1.

Palanti, L., Puggelli, S., Langone, L., Andreini, A., Reveillon, J., Duret, B., Demoulin, F.X., 2021. An attempt to predict spray characteristics at early stage of the atomization process by using surface density and curvature distribution. Int. J. Multiph. Flow. 147, 103879. http://dx.doi.org/10.1016/j.ijmultiphaseflow.2021.103879.

Payri, R., Gimeno, J., Martí-Aldaraví, P., Carvallo, C., 2020. Parametrical study of the dispersion of an alternative fire suppression agent through a real-size extinguisher system nozzle under realistic aircraft cargo cabin conditions. Process Saf. Environ. Prot. 141, 110–122. http://dx.doi.org/10.1016/j.psep.2020.04.022.

Payri, R., Gimeno, J., Martí-Aldaraví, P., Martínez, M., 2022. Transient nozzle flow analysis and near field characterization of gasoline direct fuel injector using Large Eddy Simulation. Int. J. Multiph. Flow. 148, http://dx.doi.org/10.1016/j.ijmultiphaseflow.2021.103920.

Pope, S.B., 2000. Turbulent Flows. Cambridge University Press, Cambridge, http://dx.doi.org/10.1017/CBO9780511840531.

Popinet, S., 2009. An accurate adaptive solver for surface-tension-driven interfacial flows. J. Comput. Phys. 228 (16), 5838–5866. http://dx.doi.org/10.1016/j.jcp.2009.04.042.

Sauer, B., Sadiki, A., Janicka, J., 2014. Numerical analysis of the primary breakup applying the embedded DNS approach to a generic prefilming airblast atomizer. J. Comput. Multiphase Flows 6 (3), 179–192. http://dx.doi.org/10.1260/1757-482X.6.3.179.

Sauer, B., Sadiki, A., Janicka, J., 2016. Embedded DNS concept for simulating the primary breakup of an airblast atomizer. At. Spray. 26 (3), 187–217. http://dx.doi.org/10.1615/AtomizSpr.2014011019.

Scardovelli, R., Zaleski, S., 2003. Interface reconstruction with least-square fit and split Eulerian-Lagrangian advection. Internat. J. Numer. Methods Fluids 41 (3), 251–274. http://dx.doi.org/10.1002/fld.431.

Schroeder, W., Martin, K., Lorensen, B., 2018. The visualization toolkit (VTK). Open Source.

Sethian, J.A., 1996. A fast marching level set method for monotonically advancing fronts. Proc. Natl. Acad. Sci. 93 (4), 1591–1595. http://dx.doi.org/10.1073/pnas.93.4.1591.

Søvde, O.A., Matthes, S., Skowron, A., Iachetti, D., Lim, L., Owen, B., Hodnebrog, Ø., Genova, G.D., Pitari, G., Lee, D.S., Myhre, G., Isaksen, I.S.A., 2014. Aircraft emission mitigation by changing route altitude: A multi-model estimate of aircraft NOx emission impact on O3 photochemistry. Atmos. Environ. 95, 468–479. http://dx.doi.org/10.1016/j.atmosenv.2014.06.049.

Torregrosa, A.J., Payri, R., Salvador, F.J., Crialesi-Esposito, M., 2020. Study of turbulence in atomizing liquid jets. Int. J. Multiph. Flow. 129, 103328. http://dx.doi.org/10.1016/j.ijmultiphaseflow.2020.103328.

Tryggvason, G., Scardovelli, R., Zaleski, S., 2011. Direct Numerical Simulations of Gas–Liquid Multiphase Flows, first ed. Cambridge University Press, http://dx.doi.org/10.1017/CBO9780511975264.

Valdés, R.M.A., Burmaoglu, S., Tucci, V., da Costa Campos, L.M.B., Mattera, L., Comendador, V.F.G., 2019. Flight path 2050 and ACARE goals for maintaining and extending industrial leadership in aviation: A map of the aviation technology space. Sustainability 11 (7), 2065. http://dx.doi.org/10.3390/su11072065.

van Leer, B., 1974. Towards the ultimate conservative difference scheme. II. Monotonicity and conservation combined in a second-order scheme. J. Comput. Phys. 14 (4), 361–370. http://dx.doi.org/10.1016/0021-9991(74)90019-9.

Wardle, K.E., Weller, H.G., 2013. Hybrid multiphase CFD solver for coupled dispersed/segregated flows in liquid-liquid extraction. Int. J. Chem. Eng. 2013, 1–13. http://dx.doi.org/10.1155/2013/128936.

Warncke, K., Gepperth, S., Sauer, B., Sadiki, A., Janicka, J., Koch, R., Bauer, H.J., 2017. Experimental and numerical investigation of the primary breakup of an airblasted liquid sheet. Int. J. Multiph. Flow. 91, 208–224. http://dx.doi.org/10.1016/j.ijmultiphaseflow.2016.12.010.

Warncke, K., Sadiki, A., Janicka, J., 2019. New insights in the role of turbulence for simulating primary breakup of prefilming airblast atomization. In: ILASS - Europe 2019, 29th European Conference on Liquid Atomization and Spray Systems. Paris, France.

Weller, H.G., Tabor, G., Jasak, H., Fureby, C., 1998. A tensorial approach to computational continuum mechanics using object-oriented techniques. Comput. Phys. 12 (6), 620. http://dx.doi.org/10.1063/1.168744.

White, F.M., 2006. Viscous Fluid Flow, third ed. McGraw-Hill, Singapore.

Zalesak, S.T., 1979. Fully multidimensional flux-corrected transport algorithms for fluids. J. Comput. Phys. 31 (3), 335–362. http://dx.doi.org/10.1016/0021-9991(79)90051-2.

Zandian, A., Sirignano, W.A., Hussain, F., 2017. Planar liquid jet: Early deformation and atomization cascades. Phys. Fluids 29 (6), 062109. http://dx.doi.org/10.1063/1.4986790.